Postprint of: Sun X., You W., Xuan X., Ji L., Xu X., Wang G., Zhao S., Boczkaj G., Yoon J., Chen S., Effect of the Cavitation Generation Unit Structure on the Performance of an Advanced Hydrodynamic Cavitation Reactor for Process Intensifications, CHEMICAL ENGINEERING JOURNAL, Vol. 412 (2021), 128600, DOI: 10.1016/j.cej.2021.128600

Effect of the Cavitation Generation Unit Structure on the Performance of an Advanced Hydrodynamic Cavitation Reactor for Process Intensifications

Xun Sun [a,b], Weibin You [a,b], Xiaoxu Xuan [a,b*], Li Ji [a,b], Xingtao Xu [c], Guichao Wang [a,b], Shan Zhao [d], Grzegorz Boczkaj [e], Joon Yong Yoon [f], and Songying Chen [a,b*]

[a] *Key Laboratory of High Efficiency and Clean Mechanical Manufacture, Ministry of Education, School of Mechanical Engineering, Shandong University, Jinan 250061, China*

[b] *National Demonstration Center for Experimental Mechanical Engineering Education, Shandong University, Jinan 250061, China*

[c] *International Center for Materials Nanoarchitectonics (WPI-MANA), National Institute for Materials Science, Ibaraki 305-0044, Japan*

[d] *Shandong Key Laboratory of Water Pollution Control and Resource Reuse, School of Environmental Science and Engineering, Shandong University, Qingdao 266237, China*

[e] *Department of Process Engineering and Chemical Technology, Faculty of Chemistry, Gdańsk University of Technology, Gdańsk 80-233, Poland*

[f] *Department of Mechanical Engineering, Hanyang University, Ansan 15588, Republic of Korea*

[1]xunsun@sdu.edu.cn [2]202014302@mail.sdu.edu.cn [3]xiaoxuxuan@sdu.edu.cn

[4]liji@sdu.edu.cn [5]XU.Xingtao@nims.go.jp [6]wanggc@sdu.edu.cn

[7]szhao@sdu.edu.cn [8]grzegorz.boczkaj@pg.edu.pl [9]joyoon@hanyang.ac.kr

[10]chensy66@sdu.edu.cn

Corresponding authors

Xiaoxu Xuan and **Songying Chen**

Key Laboratory of High Efficiency and Clean Mechanical Manufacture, Ministry of Education, School of Mechanical Engineering, Shandong University
National Demonstration Center for Experimental Mechanical Engineering Education, Shandong University
17923, Jingshi Road, Jinan, Shandong Province, 250061, People's Republic of China

Tel. + 86-0531-88392378

Fax + 82-0531-88392378

Email xiaoxuxuan@sdu.edu.cn and chensy66@sdu.edu.cn

Word Count: 6056

Abstract

The advanced rotational hydrodynamic cavitation reactors (ARHCRs) that appeared recently have shown obvious advantages compared with conventional devices in process intensifications. In ARHCRs, the cavitation generation unit (CGU) located on the rotor and stator basically determines their performance. For the first time, the present study investigated the effect of the CGU structure on the performance of a representative ARHCR by utilizing computational fluid dynamics. The amount of generated cavitation and required torque of the axis for various shapes, diameters, interaction distances, heights, and inclination angles of the CGU were analyzed. The results indicate that the interaction-type ARHCR (cavitation is generated by stator-rotor interaction) was far superior to the non-interaction type one. In addition, the hemisphere-shaped CGU demonstrates the best performance compared with that with cone-cylinder, cone, and cylinder shapes. Moreover, by evaluating the effects of various geometrical factors, the hemisphere-shaped CGU with a diameter of 12 mm, interaction distance of 1 mm, height of 1 mm, and inclination angle of 10° achieved the highest performance. The reasons leading to different performance were elaborated in accordance with the flow and pressure field distributions, as well as the generated cavitation patterns. The findings of this work can strongly support the fundamental understanding, design, and application of ARHCRs for process intensifications.

Keywords*: Hydrodynamic cavitation reactor; Numerical simulation; CGU structure; Cavitation generation efficiency; Process intensification*

1. Introduction

Cavitation is a rapid phase-change phenomenon consisting of the formation, growth, and subsequent collapse of cavitation bubbles in a liquid medium. During cavitational collapse, huge energy, including intense mechanical, thermal, and chemical effects, can be released into surrounding liquids. This process creates extraordinary conditions of pressures of ~1000 bar, local hotspots with ~5000 K, and high reduction and oxidation (H· and OH· can be produced by the chemical transformation of water molecules) in room environment [1]. This kind of sonochemistry effect induced by cavitation can be effectively applied to a large number of process intensifications, such as emulsification, extraction, degradation, synthesis, and catalysis, for improving treatment effectiveness, eliminating the need for extra costly solvents, and reducing the requirements for reaction conditions (e.g., temperature, pressure, concentration, and purity) [2-4].

The sonochemistry effect can be easily generated by ultrasound (i.e., acoustic cavitation, abbreviated as AC) [5], which was discovered by Richards and Loomis as early as 1927 [6]. Since the 1980s, AC technology has rapidly developed and now has been widely utilized in small-scale applications. Due to the limitation of ultrasound propagation and the high equipment cost, AC is not suitable for large-scale industrial applications in terms of the current device technology [7]. On the contrary, hydrodynamic cavitation (HC), which offers the advantages of good scalability and inexpensive device, has shown the similar treatment mechanism to that of AC in various

applications [8], such as degradation of organic compound [9], microbial inactivation (water disinfection [10] and cell disruption [11]), waste-activated sludge treatment [12], biofuel synthesis [13], refining of cellulose pulp [14], nanoparticle dispersion [15], extraction [16], flotation [17], surface finishing [18], viscosity reduction [19], nanomaterial synthesis [20], improvement of food property [21], depolymerization [22], liposome destruction [23], emulsification [24], and cotton bleaching [25]. Moreover, due to the extraordinary conditions created by sonochemistry, HC can be effectively combined with other physical or chemical techniques, e.g., AC [26], electrochemical [27], oxidation [28], catalyst [29], ultraviolet [30], and biological methods [31]. Therefore, HC technology is widely considered to have great potential for industrial-scale process intensifications [32].

Process parameters, e.g., energy input, dosage, time, pH, or temperature, can largely influence the treatment effectiveness of HC technology, which have been extensively investigated in the previous studies. Nevertheless, the most important issue for HC technology is the design of high-performance hydrodynamic cavitation reactors (HCRs) [33]. So far, various categories of HCRs have been employed to achieve the sonochemistry effect: Venturi tube [34], orifice plate [35], high-pressure homogenizer [36], high-speed homogenizer [37], liquid whistle reactor [38], swirling jet reactor [39], and vortex diode [40], etc. Recently, several advanced rotational HCRs (ARHCRs) with the performance far beyond that of conventional HCRs have been presented, however, the amount of the mechanism research on the ARHCRs themselves is considerably

limited. Specifically, even though several researchers investigated the characteristics of ARHCRs by experimental flow visualization [10, 14, 41-46], computational fluid dynamics (CFD) [47], and characteristic experiment [10, 41, 44, 45], it is still far from complete due to the lacks of the corresponding mechanisms and the design criteria of ARHCRs. For ARHCRs, the cavitation generation unit (CGU) located on the rotor and stator is the most essential element, therefore, its geometrical structure is extremely vital for the cavitation generation, as well as effectiveness and economic efficiency. Nevertheless, to the best of our knowledge, no experimental or numerical work on the effect of CGU structure on the performance has been published in the past, which largely influencing the further investigations on the geometrical optimization and design of ARHCRs, as well as the development of HC technology.

Recently, we successfully discovered the cavitation generation mechanism and cavitation development process of a representative ARHCR [10, 12, 44, 45, 48] by utilizing a new CFD strategy which simplified the interaction flow region between the rotor and cover to 1/32 of the full flow path [49]. In this study, we investigated the effect of CGU structure on the ARHCR performance by employing this CFD strategy for the first time. The effects of shapes, diameters, interaction distances, heights, and inclination angles of the CGU on the amount of cavitation generation and energy consumption were revealed. By analyzing the flow and pressure fields, the reasons leading to different performance were discussed. The findings will provide strong support to the fundamental understanding, design, and application of ARHCRs in

process intensifications.

2. Numerical Method

2.1 Governing Equations

In the Euler-Euler approach, various phases are mathematically treated as interpenetrating continua by deriving a set of equations characterized by volume fractions of each phase from conservation equations. As one of the most representative models in the Euler-Euler approach, the mixture model predicts fluid and gas phases by solving the continuity and momentum equation for the mixture, and the volume fraction equations for the secondary phases. The continuity and momentum equations for the mixture are as follows [50].

$$\frac{\partial}{\partial t}\left(\rho_m\right)+\nabla\cdot\left(\rho_m\vec{v}_m\right)=0 \tag{1}$$

$$\frac{\partial}{\partial t}\left(\rho_m\vec{v}_m\right)+\nabla\cdot\left(\rho_m\vec{v}_m\vec{v}_m\right)=-\nabla p+\nabla\cdot\left[\mu_m\left(\nabla\vec{v}_m+\vec{v}_m^{T}\right)\right]+\rho_m\vec{g}+\vec{F} -\nabla\cdot\left(\sum_{k=1}^{n}\alpha_k\rho_k\vec{v}_{dr,k}\vec{v}_{dr,k}\right) \tag{2}$$

where $\vec{v}_m$ is the mass-averaged velocity, ρ_m is the mixture density, μ_m is the viscosity of the mixture, n is the number of phases, α_k is the volume fraction of phase, and $\vec{v}_{dr,k}$ is the drift velocity for secondary phase.

2.2 Turbulence and Cavitation models

To accurately predict the turbulence behavior of different categories of fluid flows, choosing an appropriate turbulence model is the most important issue in CFD numerical simulations [51]. The Reynolds-Averaged Navier-Stokes (RANS) turbulence models, basing on the Boussinesq eddy viscosity assumption, have shown their advantages in a

great number of industrial applications [52]. The shear stress transport (SST) k-omega model, which combines the advantages of the standard k-epsilon and standard k-omega models, has been successfully applied to cavitating flows which are characterized by highly unsteady and strong separation features [53], because of reasonable accuracy and cost. Even though the large eddy simulation (LES) normally yields better quantitative agreement with experimental data than the RANS models [54], even nowadays the LES requires several orders of magnitude more CPU time than RANS models [55]. Therefore, the SST k-omega model was used to predict the cavitating flows in the ARHCR in the present study. The description of the SST k-omega model can be found in the study by Menter [56] and is not repeated here.

The Schnerr-Sauer model, which derives the exact expression for the net mass transfer from liquid to vapor, was utilized to model the cavitation flow behavior [57]. The liquid-vapor mass transfer in this model is defined as follows.

$$R = \frac{\rho_V \rho_l}{\rho} \alpha (1-\alpha) \frac{3}{\Re_B} \sqrt{\frac{2}{3} \frac{P_V - P}{\rho_l}} \tag{3}$$

where $\Re_B$ is the bubble radius:

$$\Re_B = \left(\frac{\alpha}{1-\alpha} \frac{3}{4\pi} \frac{1}{n} \right)^{1/3} \tag{4}$$

2.3 Solver Setup

In the present study, the commercial CFD code ANSYS Fluent 18.2 was applied to predict the cavitating flow in the ARHCR. The incompressible Navier-Stokes equations were discretized by utilizing the finite volume method with double precision. To

robustly derive the additional condition for pressure by reformatting the continuity equation, the Coupled scheme was used to achieve the pressure-velocity coupling. For the spatial discretization, the QUICK scheme was applied to the momentum and volume fraction equations. The second-order upwind scheme was used for the turbulence kinetic energy and turbulence dissipation rate equations, together with the PRESTO! interpolation scheme for pressure. To ensure the stability of the iteration, the flow courant number was specified as 50 and the under-relaxation factors in the vaporization mass and volume fraction equations were adjusted to 0.1 [49].

To achieve reliable results, five interaction cycles (0.5 ms/cycle) with a time step of 0.0625 ms were conducted for each case. Because the total vapor volume varies (normally increases) as the iteration progresses, the convergence criterion for each time step was specified as no variation in the total vapor volume, instead of using any residual of the flow or turbulent properties. This criterion can be achieved after 500 iterations for each time step, meanwhile, all the residuals can reduce to less than 10^{-6}. Therefore, the numbers of the total time step and iteration per time step were specified as 40 and 500, respectively [49].

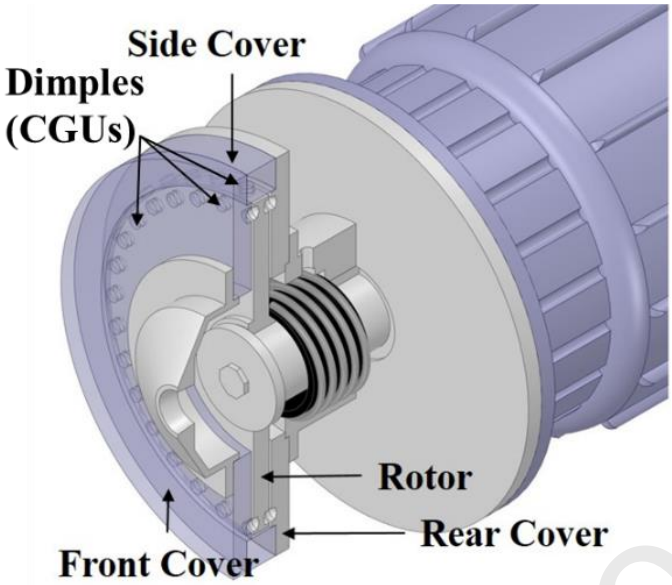

Fig. 1 Schematic diagram of the ARHCR [48].

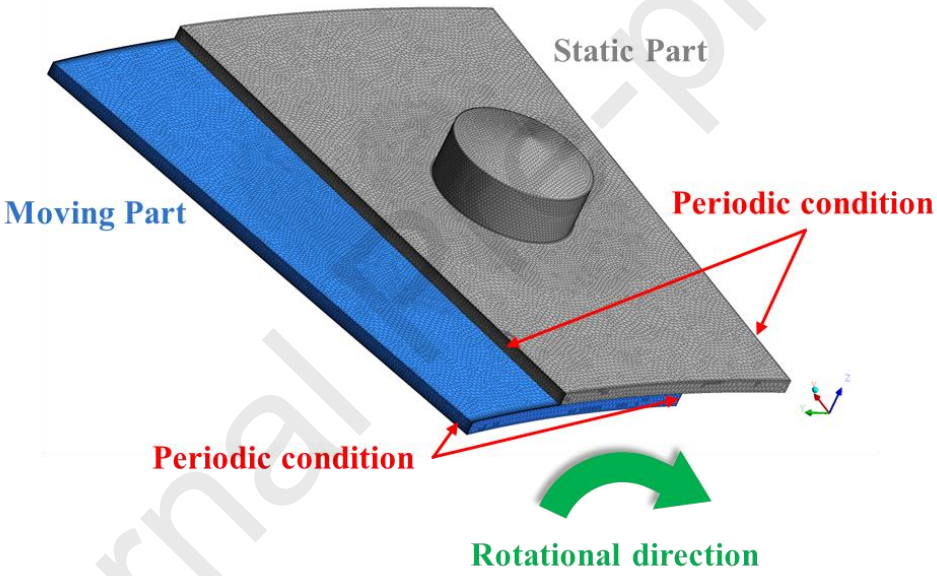

Fig. 2 Computational domain and boundary conditions of the simplified model of the ARHCR [49].

2.4 Computational Domain and Boundary Conditions

The ARHCR contained a front cover, rotor, side cover, and rear cover, as shown in Fig. 1. 32 cone-cylinder-shaped CGUs with a diameter of 10 mm and a height of 3.5 mm were processed on the surface of the rotor, front cover, and rear cover in a single

row, respectively, equally spaced. The detailed description can be found in our previous research [48]. Because the cavitation flow field and geometry of the ARHCR periodically change, the full flow path can be simplified to 1/32 of the interaction region as the computational domain for each case (Fig. 2), as confirmed in our previous study [49]. The structure of the original model was identical to the real ARHCR. To eliminate the interference effect from the side walls on the flows, the length of the domain in the radial direction was specified as 40 mm which is four times the diameter of the CGU. The original interaction distance between the rotor and stator was specified as 2 mm. To reveal the effect of CGU structure on the performance, various geometrical factors, i.e., shapes (cone-cylinder, non-interaction type, cone, cylinder, and hemisphere), diameters (D = 8, 9, 10, 11, and 12 mm), interaction distances (s = 1, 1.5, 2, 2.5, and 3 mm), heights (h = 0, 0.5, 1, 1.5, and 2 mm), and inclination angles (θ = -20°, -10°, 0°, 10°, and 20°) of the CGU were investigated. The detailed information on the geometrical factors can be found in Fig. 3.

Due to the highly unsteady nature of the cavitation phenomenon, the adequate mesh category and size of the computational domain have to be ensured in numerical simulations. Because polyhedral grid offers better accuracy, convergence, and convenience compared with tetrahedral and hexahedral grids [44], it was applied to the present study for each case and was generated by combining ANSYS Meshing 18.2 and ANSYS Fluent 18.2. To meet the requirement of the low-Reynolds number boundary condition for the SST k-ω model, ten inflation layers were generated near the walls with

$Y_{plus} \approx 1$ for the first layer. To accomplish the interaction of the moving and static CGUs, the upper region (marked in grey) was specified as the static part and the bottom region (marked in blue) was specified as the moving part rotating clockwise on Z-axis with a rotational speed of -3600 rpm, as shown in Fig. 2. The surfaces of the left and right ends of each part were mutually specified as one pair of periodic conditions, respectively. All other faces were set to walls with no-slip condition and the roughness height was assumed to be zero. The saturated vapor pressure of water was set to 2064 Pa corresponding to the experiment temperature. The bubble number density was specified as 10^9 [49].

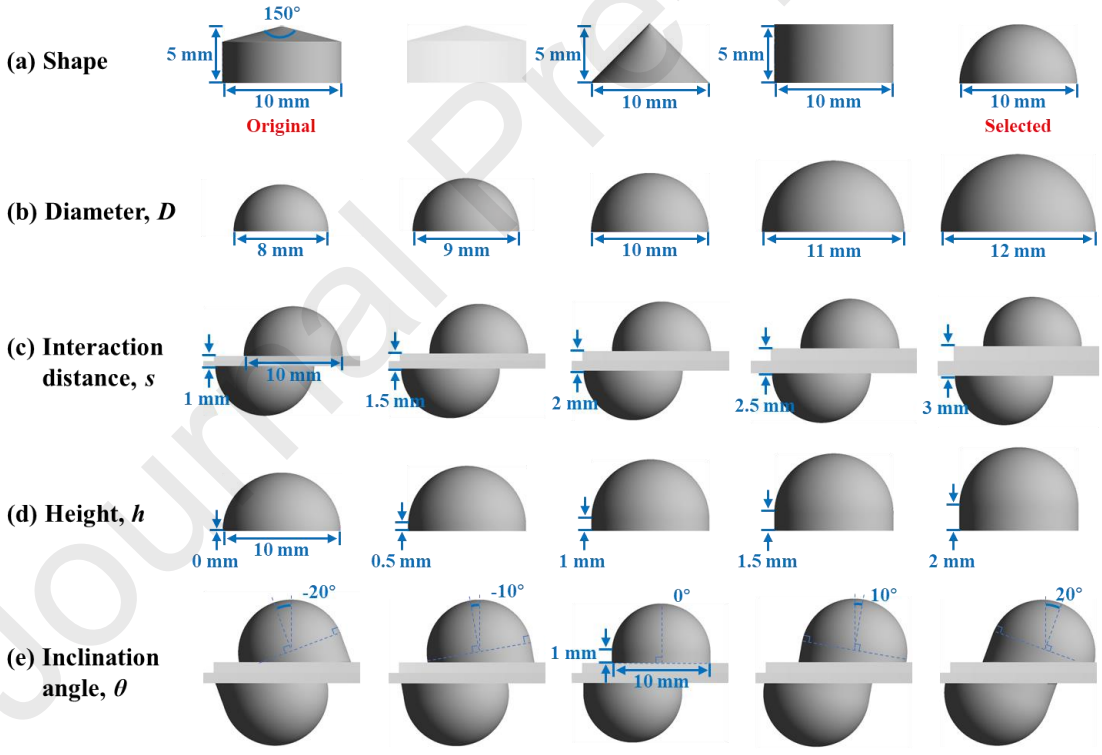

Fig. 3 Various geometrical factors of the CGU investigated in the numerical simulation.

In the present study, the total volume fraction of vapor, α_{total}, and the total torque of the rotor wall per unit volume, $\left|\overrightarrow{M}_z\right|/V_{total}$, were utilized to evaluate the performance of the simplified ARHCR. α_{total} is a convenient parameter standing for the induced cavitation intensity, which can be defined as the ratio of the total vapor volume, V_{vapor}, to the total volume of the computational domain, V_{total}:

$$\alpha_{total}=\frac{V_{vapor}}{V_{total}}=\frac{\sum_{i=1}^{N}\alpha_{vapor}V_i}{\sum_{i=1}^{N}V_i} \tag{5}$$

where N is the total number of cells in the computational domain, α_{vapor} is the vapor volume fraction of each cell, and V_i is the volume of each cell. $\overrightarrow{M}_z$, which can represent the required shaft power of the electric motor, can be calculated by summing the cross products of the pressure and viscous force vectors for each face with the moment vector:

$$\overrightarrow{M}_z=\vec{r}\times\overrightarrow{F_p}+\vec{r}\times\overrightarrow{F_v} \tag{6}$$

where $\vec{r}$ is the vector from the moment center to the force origin, $\overrightarrow{F_p}$ is the pressure force vector, and $\overrightarrow{F_v}$ is the viscous force vector.

The cavitation generation efficiency, η, can be expressed as the ratio of α_{total} to $\left|\overrightarrow{M}_z\right|/V_{total}$:

$$\eta=\frac{V_{vapor}}{\left|\overrightarrow{M_z}\right|} \tag{7}$$

Because the maximum intensity of the interaction effect appeared before the coinciding stage [49], to intuitively demonstrate the difference in the performance of

each structure, α_{vapor} and $\overrightarrow{M}_z$ in each case were obtained at 15.9375 ms.

Table 1 Results of the grid-independence test for the simplified ARHCR model.

Resolution	Maximum element size (mm)	α_{total} (%)
Coarse	3.5	1.478
Medium	2.5	1.524
Fine	1.5	1.522

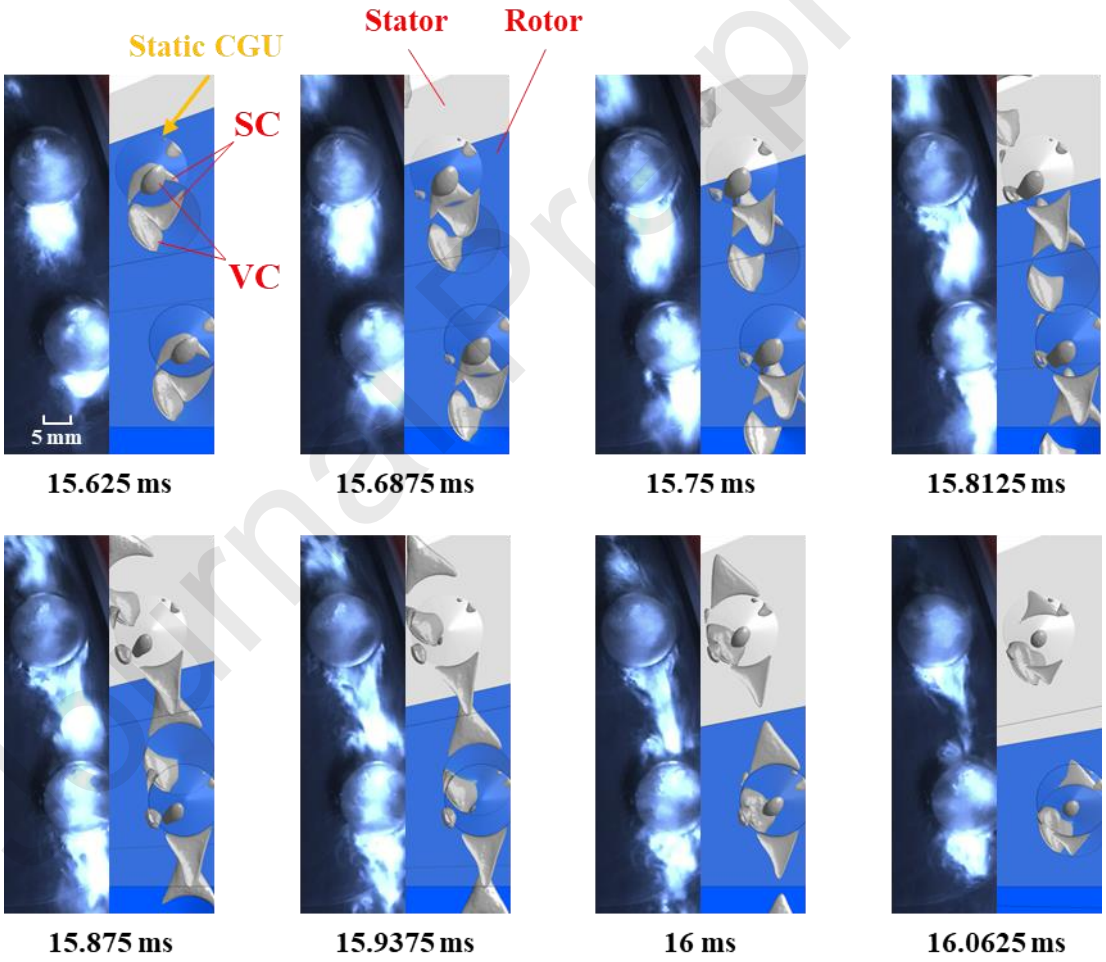

Fig. 4 Cavitation phenomenon generated by the CGUs during one interaction cycle from 15.625 to 16.0625 ms (CGU represents cavitation generation unit, SC represents sheet cavitation region, and VC represents vortex cavitation region). The left represents experimental flow visualization and the right represents numerical top view. The iso-

surfaces in grey color represent cavitation patterns with the volume fraction of gas phase at 0.1 [49, 58].

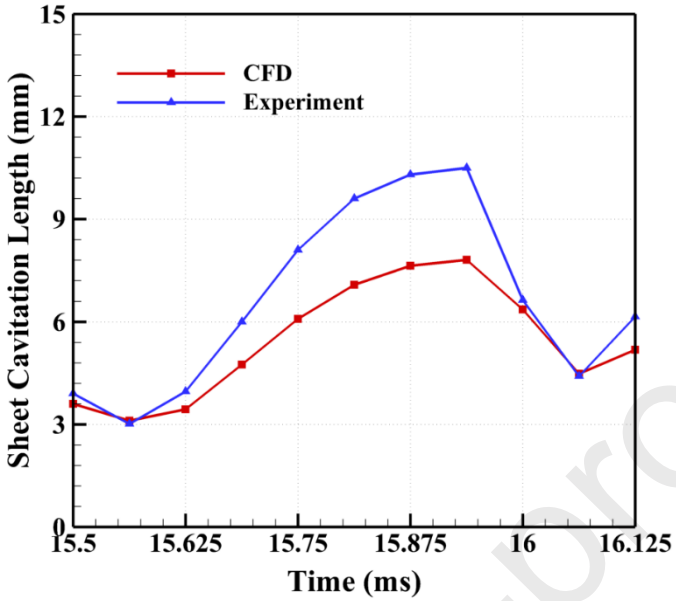

Fig. 5 Change in the sheet cavitation length (generated by the upper static CGU) in the flow region from 15.5 to 16.125 ms. (CFD results represent the length at the volume fraction of gas phase at 0.1) [49].

2.5 Grid-Independence Test and Validation of Numerical Simulation

Because the geometrical models for each case were not identical, the maximum element size was chosen as the index of the grid resolution, instead of using the total cell number. Table 1 presents the results of the grid-independence test for three mesh resolutions of the original model: coarse, medium, and fine. Because the difference of the α_{total} between the medium and fine grids was negligible, a medium grid resolution was utilized to predict the grid-independent simulation results with a consideration of economy and grid sensitivity.

To validate the correction of the numerical simulation, Fig. 4 compared the cavitation phenomenon generated by the CGUs in one interaction cycle on the top view

obtained from the experimental flow visualization (Left) and CFD (Right) [49, 58]. The sheet cavitation (SC) and vortex cavitation (VC) regions predicted by CFD marched reasonably well with the experimental observations in both time and space. In addition, to quantitatively validate the numerical method, the change in the SC length (generated by the upper static CGU predicted by CFD is compared with that of the experiment, as shown in Fig. 5 [49]. The good correlation between the numerical and experimental results demonstrate that the numerical method utilized in this study is highly believable.

3. Results and Discussions

To intuitively compare the performance of various CGU structures, Fig. 6 summarized the effects of different shapes (Fig. 6 (a)), diameters (Fig. 6 (b)), interaction distances (Fig. 6 (c)), heights (Fig. 6 (d)), and inclination angles (Fig. 6 (e)) on α_{total} and $\left|\overrightarrow{M}_z\right|/V_{total}$ at the same rotational speed, i.e., 3600 rpm. The specific values, including η, were presented in Table 2. Moreover, the effects of the corresponding structures on the velocity, vector, and pressure distributions, as well as the cavitation patterns were shown in Figs. 7–11.

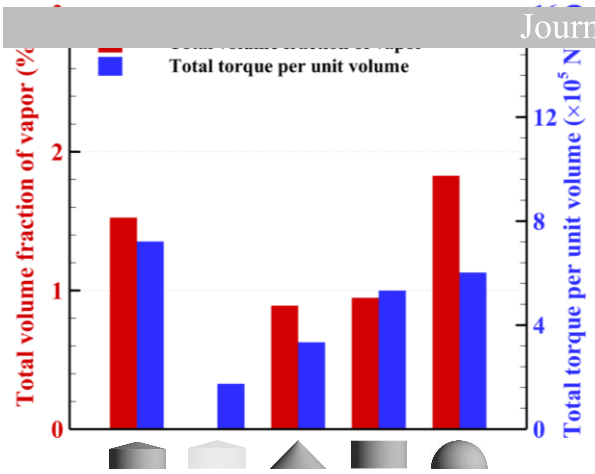

(a) Shape
(D = 10 mm, s = 2 mm, h = 0 mm, θ = 0°)

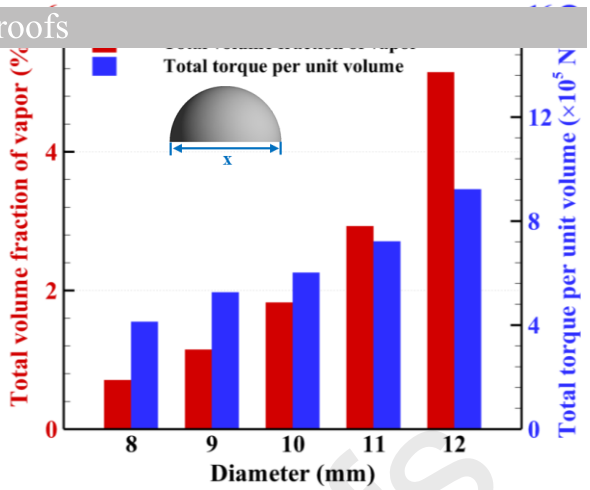

(b) Diameter
(s = 2 mm, h = 0 mm, θ = 0°)

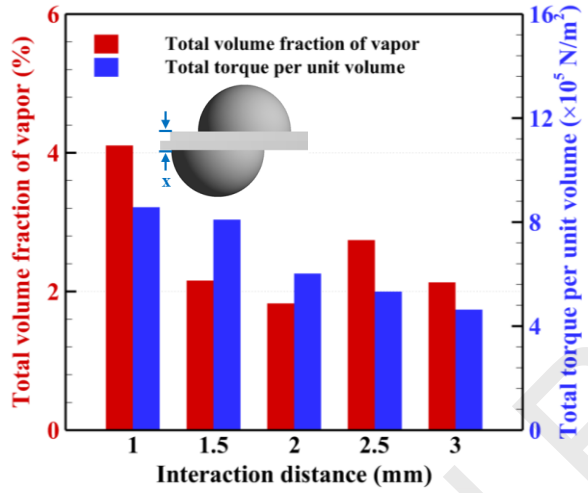

(c) Interaction distance
(D = 10 mm, h = 0 mm, θ = 0°)

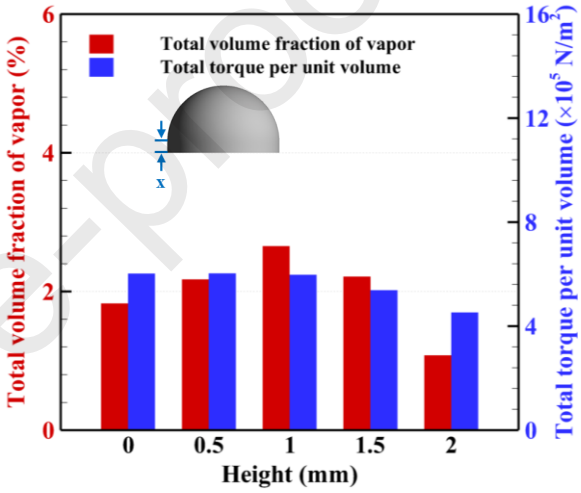

(d) Height
(D = 10 mm, s = 2 mm, θ = 0°)

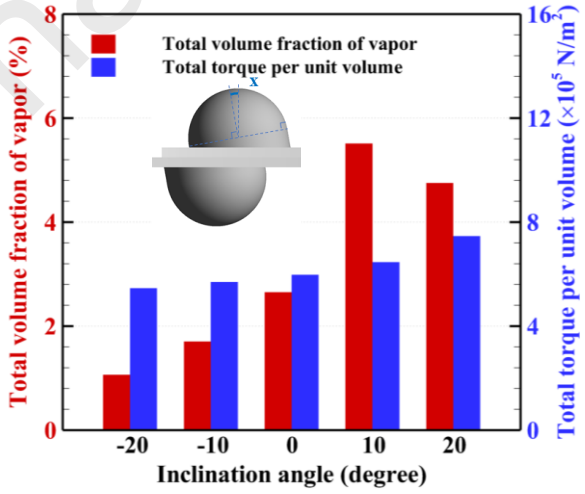

(e) Inclination angle
(D = 10 mm, s = 2 mm, h = 1 mm)

Fig. 6 Effect of various geometrical factors on the total volume fraction of vapor and total torque per unit volume.

Table 2 Effects of various geometrical factors on the performance.

	Parameters	V_{vapor} ($\times10^{-8}$ m^3)	V_{total} ($\times10^{-6}$ m^3)	α_{total} (%)	$\overrightarrow{F_p}$ (N·m)	$\overrightarrow{F_v}$ (N·m)	$\overrightarrow{M_z}$ (N·m)	$\lvert\overrightarrow{M_z}\rvert/V_{total}$ ($\times10^5$ N/m^2)	η ($\times10^{-8}$ m^2/N)
Shape	Cone-cylinder	3.878	2.544	**1.524**	1.692	0.143	1.835	**7.214**	**2.113**
	Non	0	2.234	**0**	0.282	0.108	0.390	**1.745**	**0**
	Cone	1.946	2.185	**0.890**	0.595	0.134	0.729	**3.336**	**2.669**
	Cylinder	2.567	2.709	**0.947**	1.313	0.129	1.442	**5.322**	**1.780**
	Hemisphere	4.467	2.447	**1.826**	1.329	0.143	1.472	**6.017**	**3.035**
Diameter (mm)	8	1.548	2.191	**0.707**	0.756	0.149	0.905	**4.131**	**1.710**
	9	2.641	2.305	**1.146**	1.065	0.149	1.214	**5.267**	**2.175**
	10	4.467	2.447	**1.826**	1.329	0.143	1.472	**6.017**	**3.035**
	11	7.674	2.620	**2.929**	1.753	0.138	1.891	**7.219**	**4.057**
	12	14.555	2.828	**5.147**	2.492	0.117	2.609	**9.227**	**5.578**
Interaction distance (mm)	1	6.093	1.485	**4.105**	1.114	0.158	1.272	**8.567**	**4.791**
	1.5	4.237	1.966	**2.156**	1.449	0.141	1.590	**8.091**	**2.664**
	2	4.467	2.447	**1.826**	1.329	0.143	1.472	**6.017**	**3.035**
	2.5	8.025	2.928	**2.741**	1.421	0.139	1.560	**5.328**	**5.144**
	3	7.263	3.409	**2.131**	1.444	0.134	1.578	**4.630**	**4.602**
Height (mm)	0	4.467	2.447	**1.826**	1.329	0.143	1.472	**6.017**	**3.035**
	0.5	5.490	2.525	**2.174**	1.381	0.140	1.521	**6.024**	**3.610**
	1	6.908	2.604	**2.653**	1.422	0.134	1.556	**5.976**	**4.440**
	1.5	5.936	2.682	**2.213**	1.316	0.127	1.444	**5.382**	**4.112**
	2	2.980	2.761	**1.079**	1.123	0.126	1.249	**4.523**	**2.386**
Inclination angle (°)	-20	2.756	2.594	**1.063**	1.281	0.134	1.415	**5.455**	**1.948**
	-10	4.427	2.601	**1.702**	1.346	0.135	1.481	**5.694**	**2.989**
	0	6.908	2.604	**2.653**	1.422	0.134	1.556	**5.976**	**4.440**
	10	14.330	2.601	**5.509**	1.543	0.136	1.679	**6.455**	**8.534**
	20	12.323	2.594	**4.751**	1.801	0.134	1.935	**7.459**	**6.369**

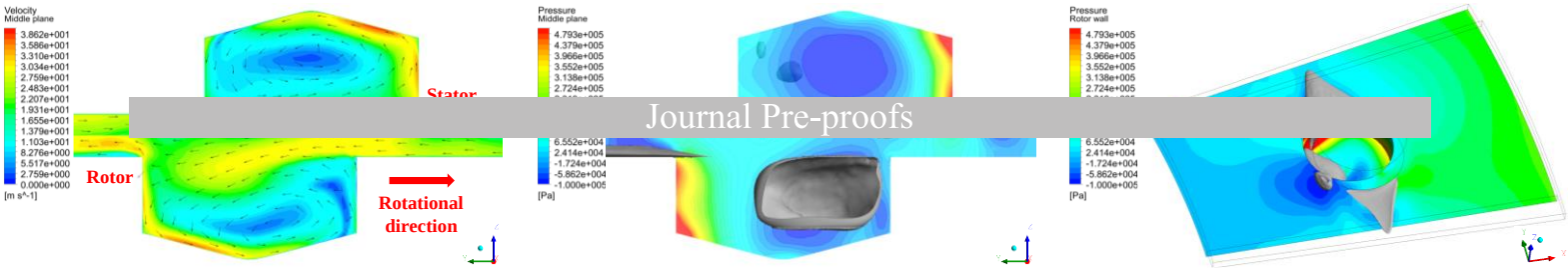

(a) Cone-cylinder

(b) Non-interaction

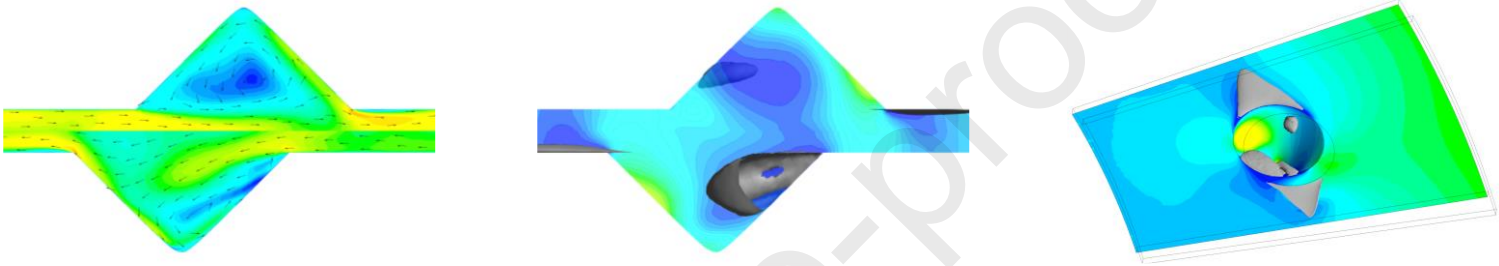

(c) Cone

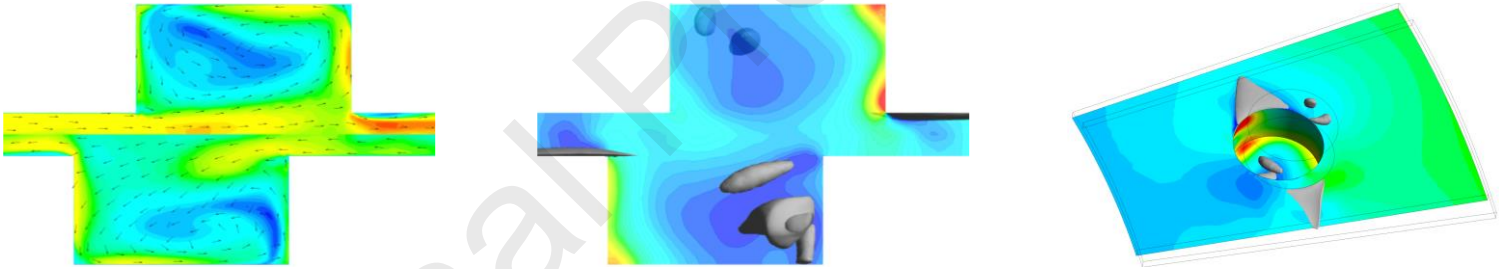

(d) Cylinder

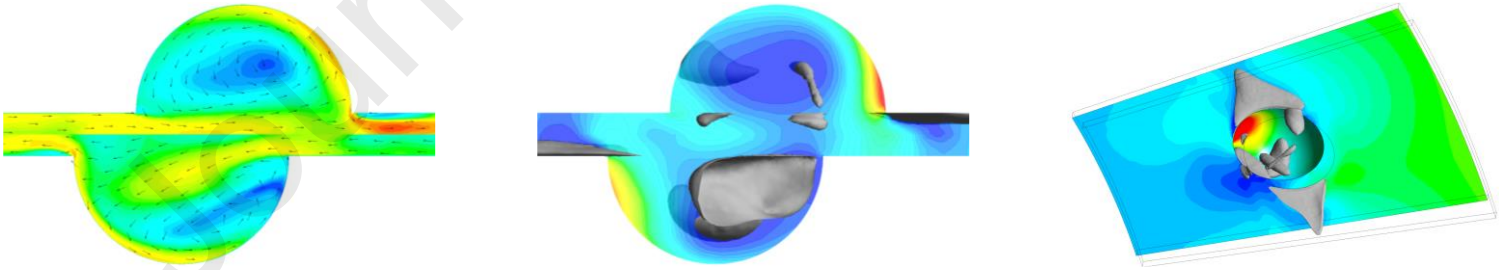

(e) Hemisphere

Fig. 7 Effect of various CGU shapes on the flow and pressure fields. The left shows the velocity and vector distributions in relative reference frame on the middle plane, the middle shows the static pressure distribution in relative reference frame on the middle plane, and the right shows the bird's-eye view with a static pressure distribution of the rotor surface. The iso-surfaces in grey color in the middle and right represent cavitation patterns with the volume fraction of gas phase at 0.2.

3.1 Effect of Shape

In accordance to the presence of CGU on stator or not, ARHCRs can be categorized into two types: interaction (i.e., cavitation is generated by the interaction motion between the stator and rotor) [46] and non-interaction (i.e., cavitation is only generated by the rotor) [59]. For the interaction type, taking the cone-cylinder-shaped CGU [48], i.e., the original structure, for an example (Fig. 7 (a)), due to viscosity the fluid in the ARHCR was driven by the rotor wall, and the flow direction was identical to the rotating direction in the absolute reference frame. The fluid in the static part (i.e., upper part) formed a vortex inside the static CGU and impacted the downstream edge of the CGU. The impact flow was suddenly veered and accelerated (from 25 to 35 m/s) and generated a separation region on the downstream side. For the fluid in the moving part, because the absolute velocity of the driven fluid was lower than the motion velocity of the rotor (i.e., 46 m/s), thus the relative flow direction was opposite to the rotor motion, which can be clearly observed in the vector distribution in relative reference frame (Fig. 7 (a) Left). Similar to the flow structure in the static part, the flow in the lower part induced the vortex and separation regions inside the moving CGU and on its downstream side. As the static pressures in the vortex and separation regions became lower than saturated vapor pressure, VC and SC regions were formed (Figs. 7 (a) Middle and Right). The upstream flow velocity in the moving part was higher than that in the static part, resulting in the higher impact and vortex velocities, and consequently, the larger VC and SC regions were formed. In addition, each high-pressure region (over

4.5×10^5 Pa) appeared at the bottom of the downstream wall of the moving CGU and on the top of the downstream wall of the static CGU, respectively, which demonstrates that the interaction effect between the stator and rotor was considerably strong (Figs. 7 (a) Middle and Right). The strong compressing effect between the two vortexes further increased the impact and vortex velocities, therefore, a well-developed vortex is conducive to the formation of both SC and VC. In summary, increasing the interaction intensity led to higher impact and vortex velocities, and consequently, higher separation and vortex intensities can be achieved. The detailed demonstration of the flow and pressure fields can be found in our previous work [49].

On the contrary, for the non-interaction type without the disturbance from the static CGU (Fig. 7 (b) Left), the upstream flow velocity (35–38 m/s) was much higher than that of the interaction type (20–30 m/s). The relative velocity in the moving part significantly was reduced from approximately 30 to 10 m/s, resulting in much lower impact and vortex velocities compared with those of the interaction type. Therefore, no obvious low-pressure or cavitation regions were formed in the CGU or on its downstream side (Figs. 7 (b) Middle and Right). Moreover, due to the minor difference in the velocity between the fluid and rotor, the maximum pressure on the downstream walls also considerably dropped to 1×10^5 Pa, which means that the interaction effect was very limited. This can be also confirmed by the pressure torque presented in Table 2: the pressure torque of the cone-cylinder shape (1.692 N·m) was 6 times that of the cone shape (0.282 N·m). Therefore, even though the interaction type required 3.13

times more $\left|\overrightarrow{M_z}\right|/V_{total}$ compared with the non-interaction type (1.745×10^5 N/m^2), the interaction-type ARHCRs, which can largely enhance the generated cavitation intensity (Fig. 6 (a)), are still a wise choice in most applications.

In the past, a number of ARHCRs with various CGU shapes, e.g., cone-cylinder [10, 60-63], cylinder [47, 64], and hemisphere [59, 65] were proposed. Figs. 7 (c)–(e) show the effects of various CGU shapes (i.e., cone, cylinder, and hemisphere) on the flow and pressure fields. For the cone-shaped CGU with a sloped wall (Fig. 7 (c)), the absence of geometrical irregular parts weakened the interaction effect between the two CGUs, leading to lower pressure on the downstream walls (3×10^5 Pa (Figs. 7 (c) Middle and Right)), velocity of the upstream flows (approximately 25 m/s (Fig. 7 (c) Left)), and pressure torque (0.595 N·m (Table 2)). Compared with the cone-cylinder shape, the generated SC regions considerably shrank because of the reduced impact velocity (from approximately 22 to 15 m/s) and the smaller separation region caused by the lesser angle of the impact flow. In addition, due to the insufficient space of the CGU and lower vortex velocity, the dimension of the induced VC regions, especially the lower one, was largely reduced. The under-developed vortexes also limited the further increase in the impact velocity. Overall, although the η of the cone-shaped CGU reached 2.669×10^{-8} m^2/N, which is 1.26 times that of the cone-cylinder shape, its α_{total} was considerably low (0.890%).

Compared with the cone-cylinder shape, the interaction intensity in the cylinder-shaped CGU was reduced, which can be confirmed by the less area of high-pressure

regions on the CGU walls (Figs. 7 (d) Middle and Right) and the lower pressure torque (1.313 N·m). Thus, both the length and the thickness of the SC regions were reduced. Moreover, the VC region in the moving CGU was largely compressed because the vortex was highly twisted, resulting from the irregular shape of the cylinder. As a result, the corresponding α_{total} and η were 0.947% and 1.780 × 10^{-8} m^2/N, respectively.

Compared with the cone-cylinder shape, the hemisphere-shaped CGU improved the α_{total} and η by 19.82% (from 1.524 to 1.826%) and 43.63% (from 2.113 to 3.035 × 10^{-8} m^2/N), respectively. This is because the smooth transition of the hemisphere shape not only formed two well-developed vortexes inside the CGUs but also largely reduced the drag force during the interaction process (Figs. 7 (e) Middle and Right). The pressure torque was reduced from 1.692 to 1.329 N·m. The stronger compressing effect between the two vortexes resulted in higher impact and vortex intensity and finally enlarged the dimension of the SC and VC regions.

Among the four categories of the CGUs, the cylinder and cone shapes have to be avoided in ARHCR designs as their considerable low α_{total} or η. The hemisphere-shaped CGU with the highest η (i.e., 3.035 × 10^{-8} m^2/N) is the primary option. In addition, the cone-cylinder shape with a η of 2.113 × 10^{-8} m^2/N is an alternative in the circumstances of limited budgets or machining conditions. Due to the lack of the experimental comparison in the previous works, the above results are needed to be validated by experimental flow visualization or characteristic experiment. Because of the high performance of the hemisphere-shaped CGU, the investigation on the effects

of diameter, interaction distance, height, and inclination angle in the next four sections is based on the hemisphere shape.

3.2 Effect of Diameter

As demonstrated in Fig. 8, increasing the diameter of the hemisphere-shaped CGU from 8 to 12 mm significantly increased the dimensions of the SC and VC regions (Figs. 8 Middle and Right), which can be attributed to the following reasons. First, the larger interaction effect between the two CGUs was induced by scaling up. The pressure torque was increased by 229.63% (from 0.756 to 2.492 N·m). Thus, both the relative and absolute areas of high-pressure regions located on the downstream walls were enlarged. Second, due to the higher interaction intensity and more sufficient space of the CGUs, the VC regions formed by the well-developed vortexes became greater and greater. In the case of 12 mm, the VC regions almost occupied the whole low-pressure regions inside the CGUs, as shown in Fig. 8 (e) Middle. Third, because of the above reasons, the impact velocity rapidly increased from 30 to 40 m/s or even higher when the diameter was increased from 8 to 12 mm (Figs. 8 Left), resulted in the longer and thicker SC regions on the downstream sides. In summary, scaling up the diameter from 8 to 12 mm increased the α_{total} by 628% (from 0.707 to 5.147%) with 1.23 times more input energy (from 4.131 to 9.227 $\times$ 10^5 N/m^2), and consequently, increased the η from 1.710 to 5.578 $\times$ 10^{-8} m^2/N, as presented in Table 2. This feature demonstrates that ARHCRs with the hemisphere-shaped CGU can be applied in industrial-scale applications as their cavitation generation efficiency increases by scaling up.

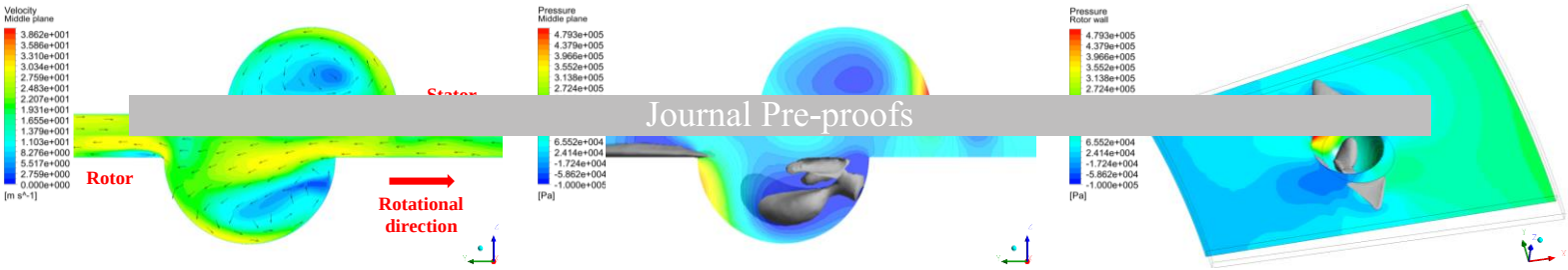

(a) d = 8 mm

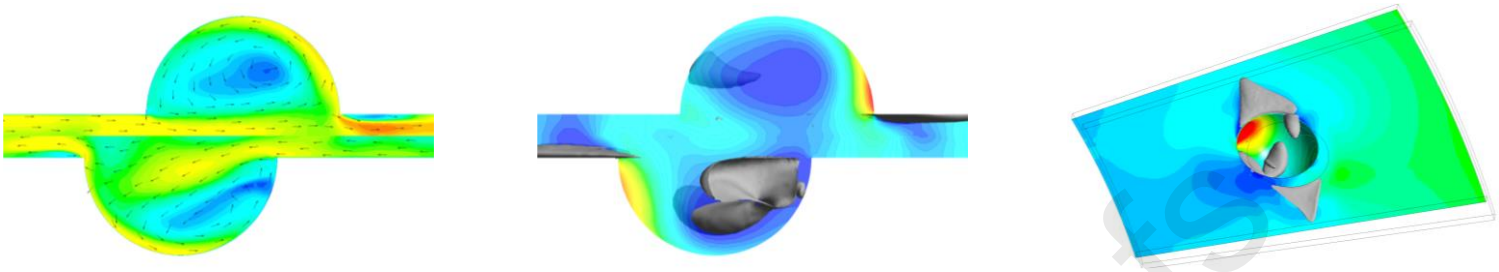

(b) d = 9 mm

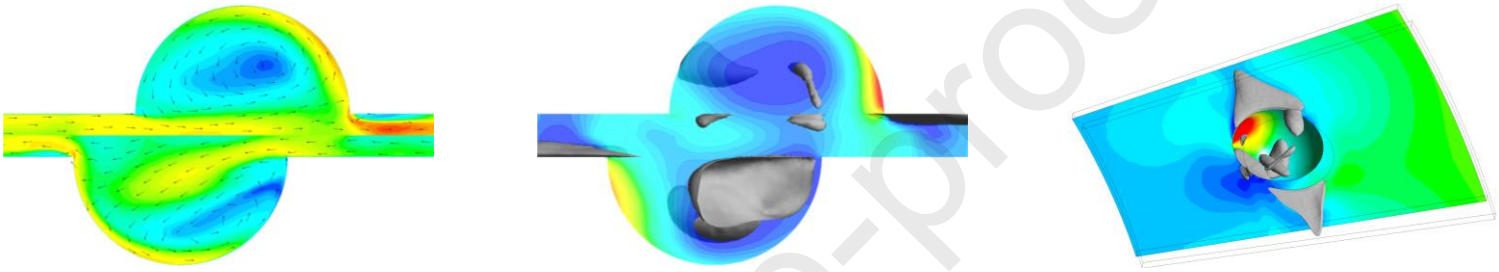

(c) d = 10 mm

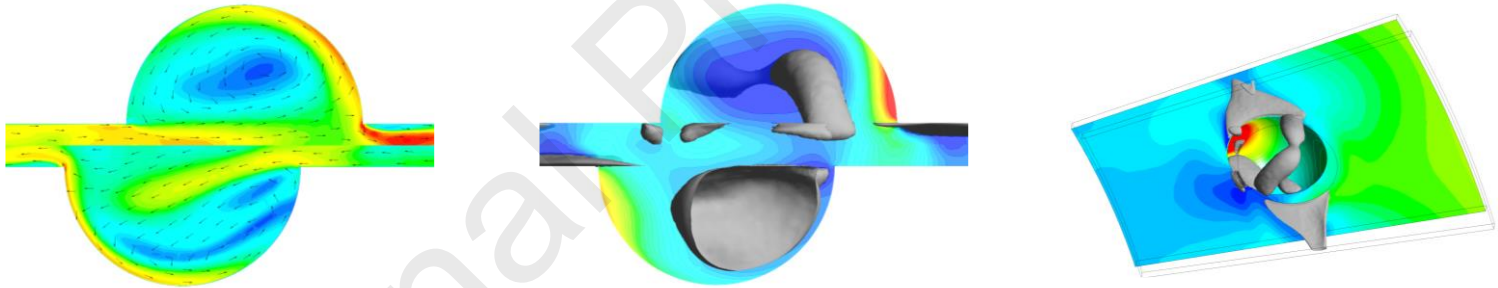

(d) d = 11 mm

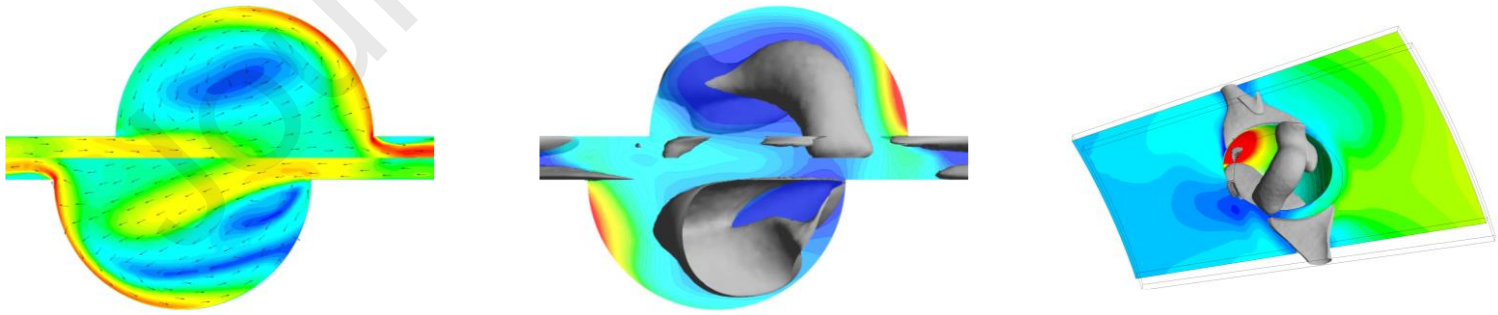

(e) d = 12 mm

Fig. 8 Effect of various CGU diameters on the flow and pressure fields, corresponding to Fig. 7.

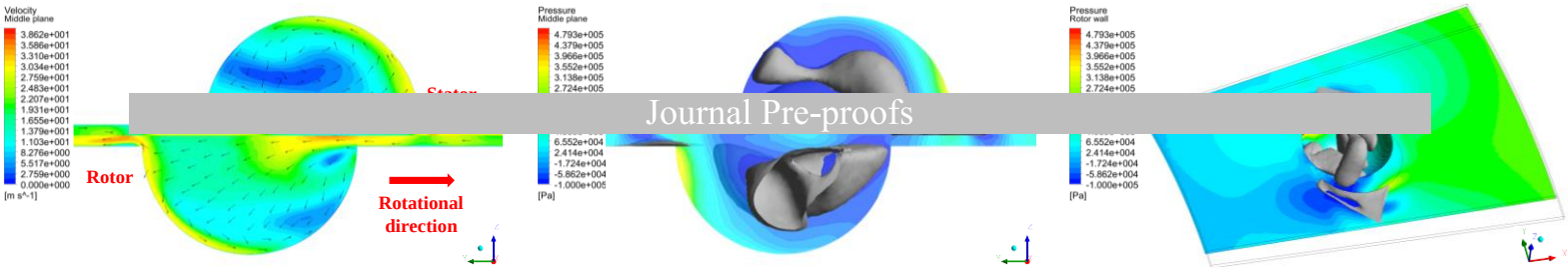

(a) s = 1 mm

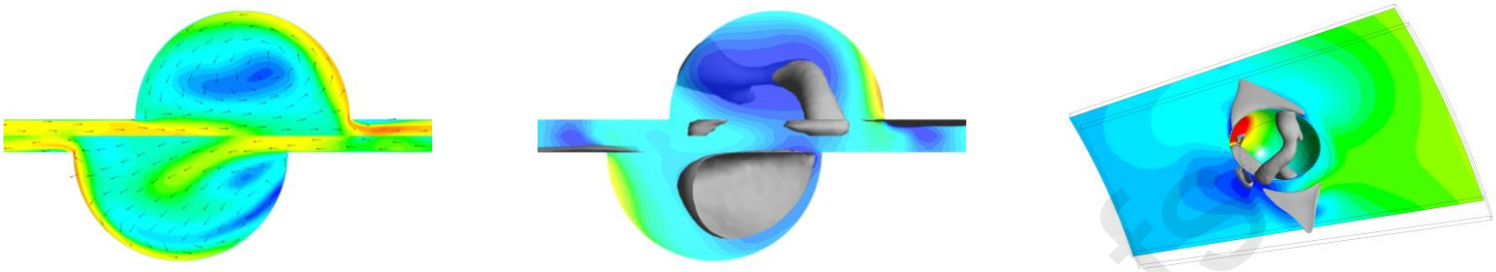

(b) s = 1.5 mm

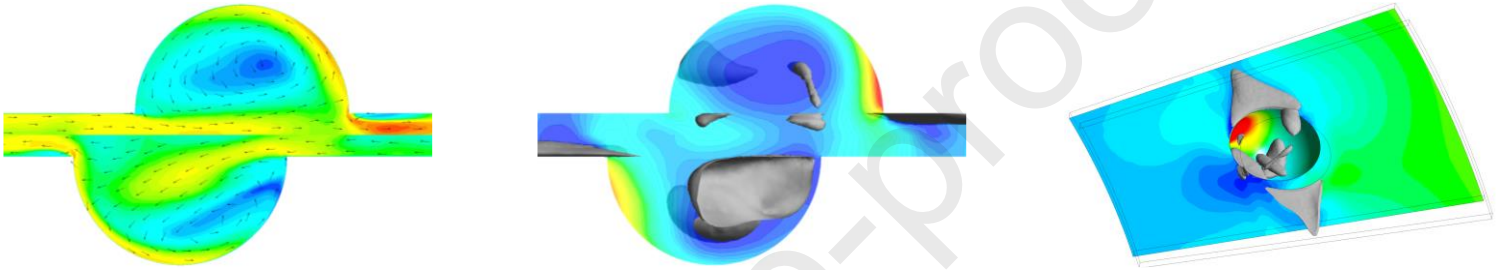

(c) s = 2 mm

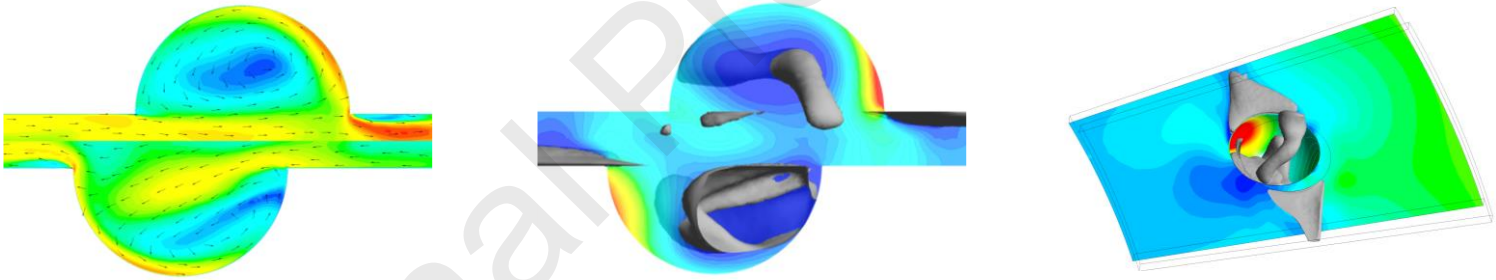

(d) s = 2.5 mm

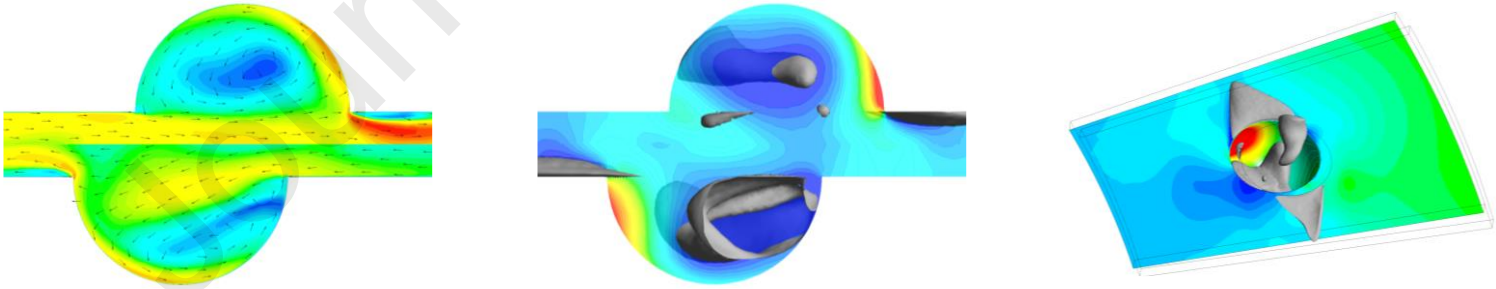

(e) s = 3 mm

Fig. 9 Effect of various interaction distances on the flow and pressure fields, corresponding to Fig. 7.

3.3 Effect of Interaction Distance

Fig. 9 indicates the effect of various interaction distances (i.e., 1, 1.5, 2, 2.5, and 3 mm) on the flow and pressure fields. The VC regions were obviously expanded by decreasing the distance from 2 to 1 mm, as shown in Figs. 9 (a)–(c) Middle and Right. The reason for this is the compressing effect between the two vortexes became much more violent, resulting in larger vortex volumes, as well as higher vortex velocities. At the same time, the narrow clearance between the rotor and stator largely limited the development of the separation regions generated by the impacting flows, which is harmful for SC generation (Figs. 9 (a)–(c) Left). In addition, due to the narrower clearance, the amount of the fluids driven by the rotor was decreased, resulting in lower demand for the rotor shaft power. This can be identified by the less area of the high-pressure regions on the downstream walls and lower pressure torque (from 1.329 to 1.114 N·m). On the whole, the ARHCR performance can be considerably improved by decreasing the interaction distance: a decrease in the distance from 2 to 1 mm gave rise to 124.81% more α_{total} (from 1.826 to 4.105%) with 13.59% less shaft power, resulting in 1.58 times η (from 3.035 to 4.791 × 10^{-8} m^2/N). This finding can be supported by Petkovšek, et al. [42] who discovered that when the distance between the rotor and stator of an interaction-type ARHCR was reduced from 3.5 to 0.8 mm, the standard deviation of the pressure inside the reactor increased two times at 2850 rpm. Moreover, the pressure amplitudes at 3.5 mm were 0.7 bar on average, while in the case of 0.8 mm the pressure amplitudes raised up to 1.7 bar.

On the other hand, the interaction effect became stronger when the distance was increased from 2 to 2.5 mm. This can be confirmed by the increased pressure torque (from 1.329 to 1.421 N·m) and area of the high-pressure regions (Figs 9. (c) and (d) Middle and Right). Therefore, the higher impact and vortex intensities resulted in larger SC and VC regions. The α_{total} was increased by 50.11% (from 1.826 to 2.741%). When the distance was increased from 2.5 to 3 mm, even the interaction intensity almost remained unchanged (from 1.421 to 1.444 N·m), however, the wider clearance between the rotor and stator weakened the compressing effect between the two vortexes, causing lower α_{total} (reduced from 2.741 to 2.131%). It can be predicted that the cavitation generation efficiency will continuously reduce by further increasing the interaction distance.

In summary, the interaction distance between the rotor and stator is an important factor affecting the performance of interaction-type ARHCRs. Narrower clearances can significantly improve the cavitation generation efficiency, however, it needs a considerably high requirement for axial or radial stability of the rotor, in order to maintain proper distance and avoid the interference between the rotor and stator. On the other hand, an appropriate increase of distance can enhance the cavitation generation efficiency and treatment capacity.

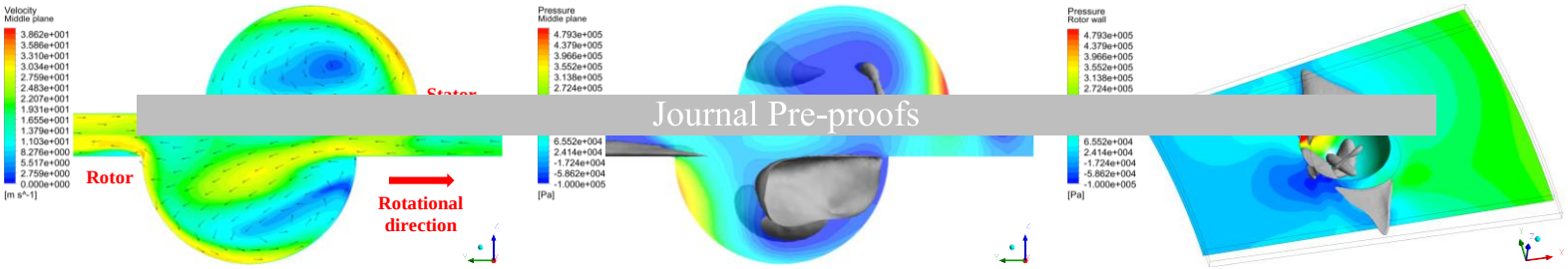

(a) h = 0 mm

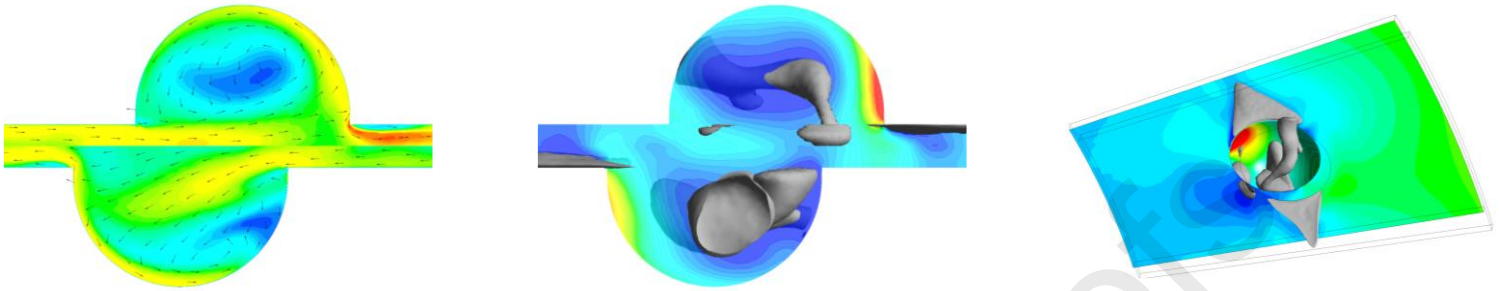

(b) h = 0.5 mm

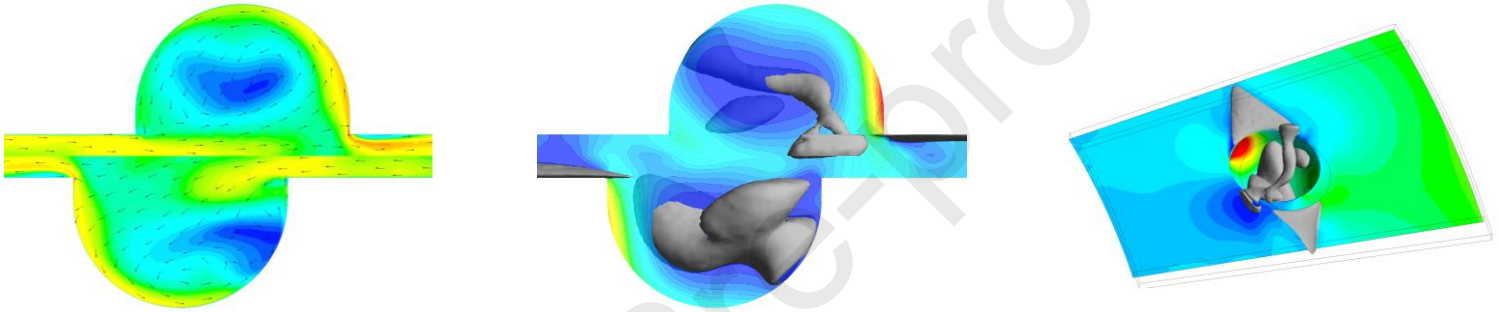

(c) h = 1 mm

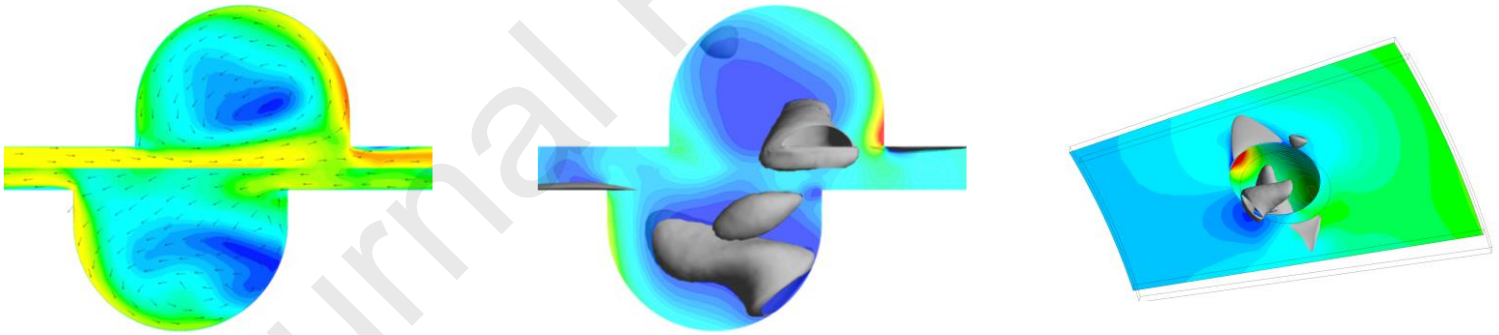

(d) h = 1.5 mm

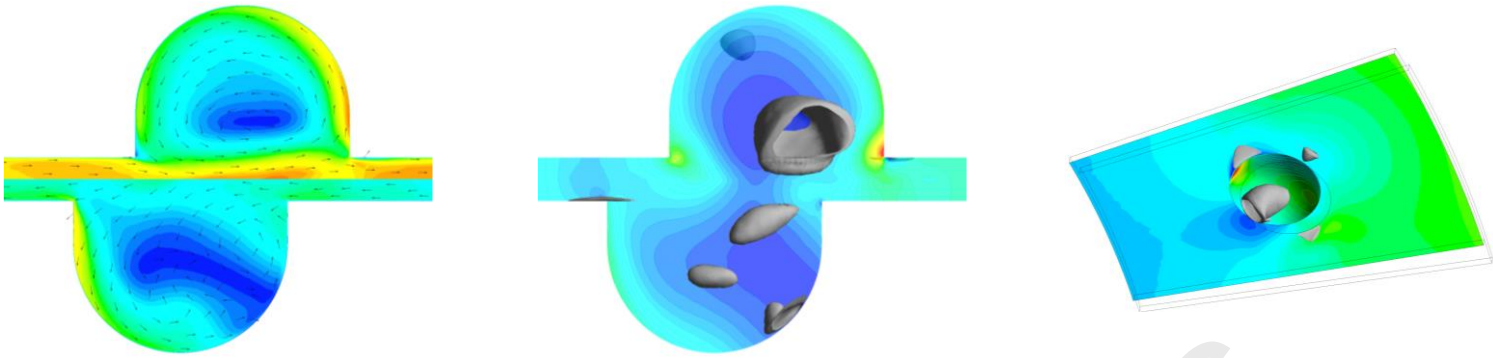

(e) h = 2 mm

Fig. 10 Effect of various heights on the flow and pressure fields, corresponding to Fig. 7.

3.4 Effect of Height

The performance of the hemisphere-shaped CGUs with various heights (i.e., 0, 0.5, 1, 1.5, and 2 mm) was shown in Fig. 10 and Table 2. The diameter, interaction distance, and inclination angle were specified as 10 mm, 2 mm, and 0°, respectively. By increasing the height from 0 to 1 mm, the α_{total} increased by 45.29% (from 1.826 to 2.653%) with a slight decrease in $\left|\overrightarrow{M}_z\right|/V_{total}$ (from 6.017 to 5.976 × 10^5 N/m^2), leading to 46.29% more η (from 3.035 to 4.440 × 10^{-8} m^2/N). This is because that the two vortexes, especially the lower one, obviously grew during this process, these two well-developed vortexes formed larger VC regions, as shown in Figs. 10 (a)–(c). In addition, the larger the vortex volume, the stronger the compressing effect, which led to greater SC regions generated by the accelerated impact flows.

On the contrary, excessively increasing the height can significantly degrade the performance. An increase in the height from 1 to 2 mm resulted in the decreases in the α_{total} and η from 2.653 to 1.079% and 4.440 to 2.386 × 10^{-8} m^2/N, respectively. The

SC regions almost disappeared on the downstream sides (Figs. 10 (e) Middle and Right). This is because that the formed vortexes in the hemisphere-shaped CGUs with excessively high height overdeveloped, the impact flow became parallel to the rotor and stator walls. With weakened interference from the CGUs, the average flow velocity largely increased (from 30 to 35 m/s), leading to much less interaction effect between the stator and rotor. This can be also confirmed by the reduction in the pressure torque from 1.422 to 1.123 N·m. As a result, the intensity and dimension of the VC regions were largely reduced.

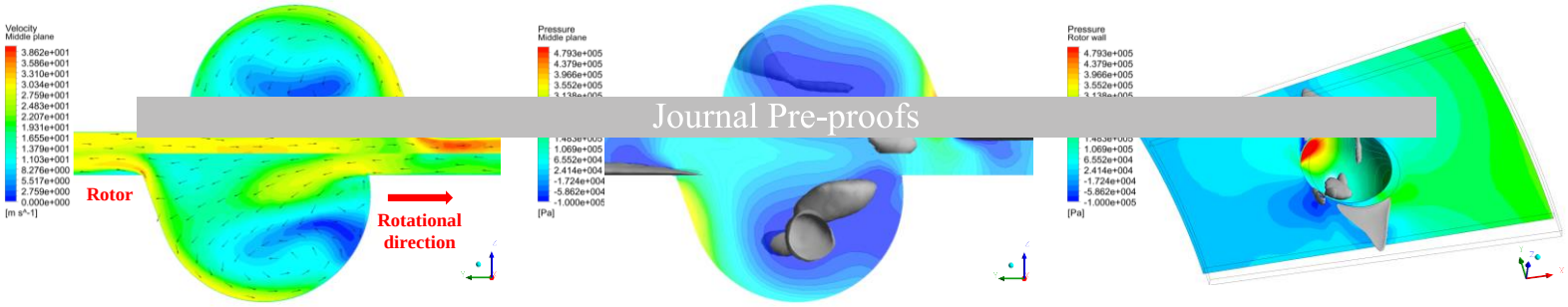

(a) θ = -20°

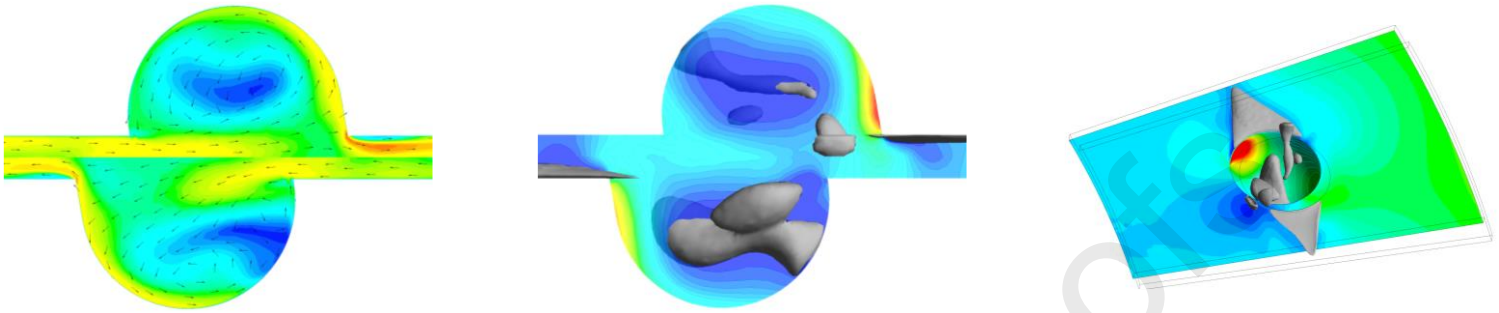

(b) θ = -10°

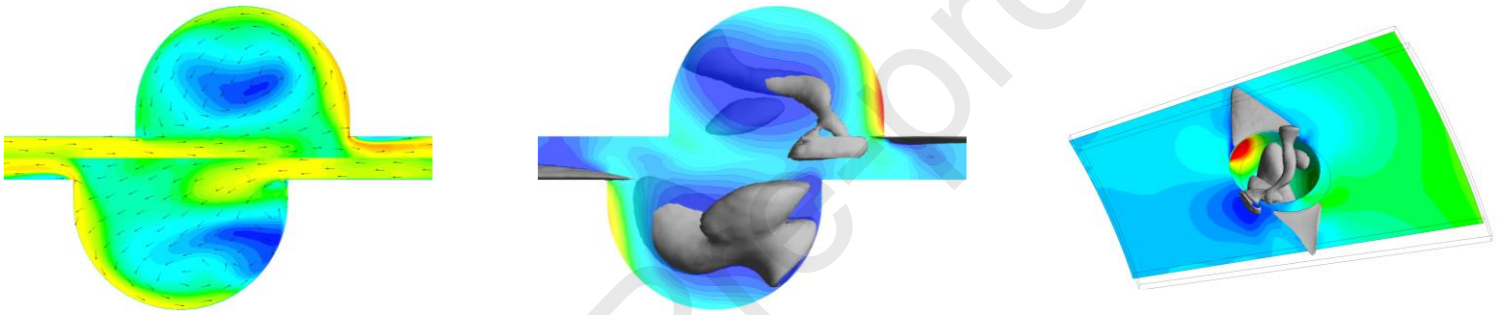

(c) θ = 0°

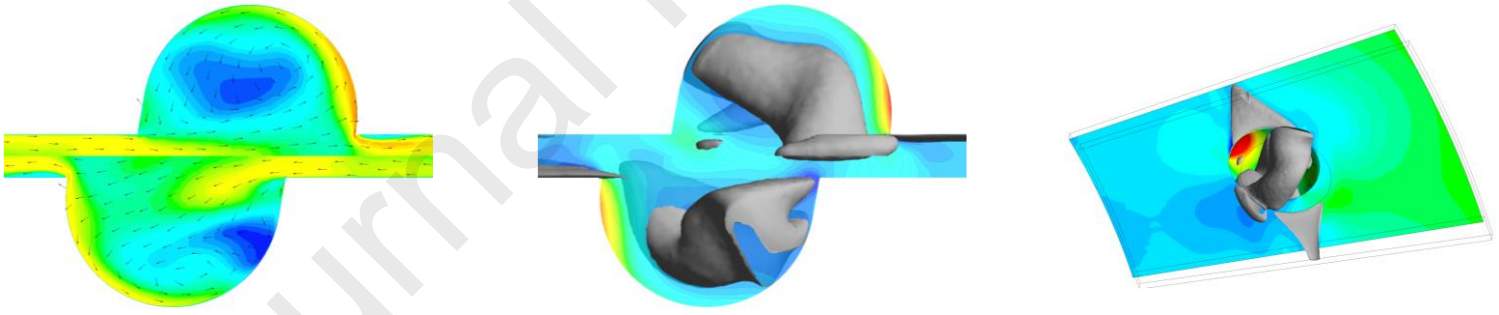

(d) θ = 10°

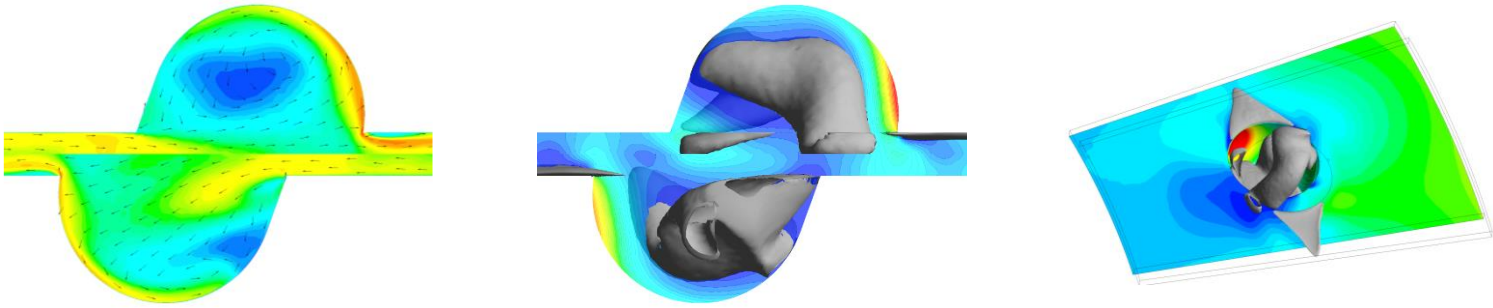

(e) θ = 20°

Fig. 11 Effect of various inclination angles on the flow and pressure fields, corresponding to Fig. 7.

3.5 Effect of Inclination Angle

The effect of inclination angle on the performance was demonstrated at five levels, i.e., -20°, -10°, 0°, 10°, and 20°. The diameter, interaction distance, and height were set to 10, 2, and 1 mm, respectively. As shown in Table 2 and Fig. 6 (e), negative inclination angles are not favorable to the cavitation generation: the α_{total} and η were reduced from 2.653 to 1.063% and from 4.440 to 1.948×10^{-8} m^2/N, respectively, by decreasing the angle from 0° to -20°. As the slope of the CGU walls was decreased, the area of the high-pressure regions on the downstream walls was shrunk (Figs. 11 (a)–(c) Middle and Right), the pressure torque was reduced from 1.422 to 1.281 N·m, which indicates that the interaction effect between the two CGUs became weaker. The lower vortex velocities (Figs. 11 (a)–(c) Left) and intensities resulted in the significant reductions in the VC regions. In addition, the slight reductions in the SC regions were caused as the impact flow was almost parallel to the rotor or stator walls.

On the other hand, compared with the CGU with 0°, the CGU with 10° improved the α_{total} by 107.65% (from 2.653 to 5.509%), with a slight increase in $\left|\overrightarrow{M}_z\right|/V_{total}$

(from 5.976 to 6.455 × 10^5 N/m^2). Because the open direction of the two CGUs was identical, the interaction effect became more intense (the pressure torque was increased from 1.422 to 1.543 N·m), resulting in higher vortex and impact velocities (Fig. 11 (d) Left) and consequently, larger VC and SC regions (Figs. 11 (d) Middle and Right). However, when the angle was increased from 10° to 20°, the required $\left|\overrightarrow{M}_z\right|/V_{total}$ was rapidly increased from 6.455 to 7.459 × 10^5 N/m^2. In addition, because the impact flows were nearly parallel to the rotor and stator walls, the development of the separation regions on the downstream sides was suppressed. The length and thickness of the SC regions were reduced. Even though the VC regions became larger due to the higher vortex velocity, the α_{total} was still decreased from 5.509 to 4.751%. It can be concluded that a small positive inclination angle is the optimal option. The Maršálek, et al. [63] were the only ones to apply the ARHCR with sloping CGUs to real applications. The effect of inclination angle on the treatment performance has not been studied in the past, which is needed to be further revealed.

4. Conclusions

The present work, for the first time, investigated the effects of CGU structures, including shapes, diameters, interaction distances, heights, and inclination angles, on the ARHCR performance by CFD. Our findings are as follows.

- The performance of interaction-type ARHCRs was much higher than that of non-interaction type ones. The hemisphere-shaped CGU showed the highest η among various common CGU shapes.

- As the CGU diameter was increased from 8 to 12 mm, the η was increased by 226.20%, which indicates the excellent scalability of ARHCRs.
- Narrow interaction distances (i.e., 1 mm) performed the best α_{total} which was approximately one time greater than that for wider distances (1.5–3 mm).
- CGUs with an appropriate height (i.e., 1 mm) increased the η by 46.29%, compared with the CGUs with no height.
- Increasing the inclination angle from 0° to 10° increased the η by 92.21%, while negative inclination angles were detrimental to cavitation generations.

The above findings can strongly contribute to the fundamental understanding, design, and application of ARHCRs in process intensifications. Nevertheless, it should be noticed that the α_{total} used in the present study may be not a proper index to characterize cavitation intensity, because it only stood for cavity size. Other more direct indexes are needed to be discovered in future. In addition, the experimental validation by real performance tests and multi-objective optimizations on the CGU structure are also required.

Acknowledgement

This work was supported by the National Natural Science Foundation of China (grant nos. 51906125, U2006221); China Postdoctoral Science Foundation (grant nos. 2020T130364, 2019M650162); Post-doctoral innovation project of Shandong Province (grant no. 202002006); Shandong Provincial Natural Science Foundation (grant no. ZR2020KB004); Youth Interdisciplinary Science and Innovative Research Groups of

Shandong University (grant no. 2020QNQT014); Young Scholars Program of Shandong University; Fundamental Research Funds of Shandong University (grant nos. 2019HW027, 2020GN050, 2019HW041); Key Research and Development Project of Zibo City (grant no. 2020XCCG0160); Ocean Industry Leading Talent Team of Yantai's Double Hundred Plan; and National Science Centre, Poland (decision no. UMO-2017/25/B/ST8/01364)

References

[1] E.B. Flint, K.S. Suslick, The Temperature of Cavitation, Science, 253 (1991) 1397-1399, https://doi.org/10.1126/science.253.5026.1397.
[2] L.H. Thompson, L.K. Doraiswamy, Sonochemistry: Science and Engineering, Ind. Eng. Chem. Res., 38 (1999) 1215-1249, https://doi.org/10.1021/ie9804172.
[3] Z. Chen, X. Xu, Z. Ding, K. Wang, X. Sun, T. Lu, M. Konarova, M. Eguchi, J.G. Shapter, L. Pan, Y. Yamauchi, Ti3C2 MXenes-derived NaTi2(PO4)3/MXene nanohybrid for fast and efficient hybrid capacitive deionization performance, Chem. Eng. J., (2020) 127148, https://doi.org/10.1016/j.cej.2020.127148.
[4] Z. Zhuge, X. Liu, T. Chen, Y. Gong, C. Li, L. Niu, S. Xu, X. Xu, Z.A. Alothman, C.Q. Sun, J.G. Shapter, Y. Yamauchi, Highly efficient photocatalytic degradation of different hazardous contaminants by CaIn2S4-Ti3C2Tx Schottky heterojunction: An experimental and mechanism study, Chem. Eng. J., (2020) 127838, https://doi.org/10.1016/j.cej.2020.127838.
[5] K. Fedorov, M. Plata-Gryl, J.A. Khan, G. Boczkaj, Ultrasound-assisted heterogeneous activation of persulfate and peroxymonosulfate by asphaltenes for the degradation of BTEX in water, J. Hazard. Mater., 397 (2020) 122804, https://doi.org/10.1016/j.jhazmat.2020.122804.
[6] W.T. Richards, A.L. Loomis, THE CHEMICAL EFFECTS OF HIGH FREQUENCY SOUND WAVES I. A PRELIMINARY SURVEY, J. Am. Chem. Soc., 49 (1927) 3086-3100, https://doi.org/10.1021/ja01411a015.
[7] X. Sun, J. Liu, L. Ji, G. Wang, S. Zhao, J.Y. Yoon, S. Chen, A review on hydrodynamic cavitation disinfection: The current state of knowledge, Sci. Total Environ., 737 (2020) 139606, https://doi.org/10.1016/j.scitotenv.2020.139606.
[8] M. Gągol, A. Przyjazny, G. Boczkaj, Effective method of treatment of industrial effluents under basic pH conditions using acoustic cavitation – A comprehensive comparison with hydrodynamic cavitation processes, Chem. Eng. Process., 128 (2018) 103-113, https://doi.org/10.1016/j.cep.2018.04.010.
[9] K. Fedorov, X. Sun, G. Boczkaj, Combination of hydrodynamic cavitation and SR-

AOPs for simultaneous degradation of BTEX in water, Chem. Eng. J., (2020) 128081, https://doi.org/10.1016/j.cej.2020.128081.

[10] X. Sun, J.J. Park, H.S. Kim, S.H. Lee, S.J. Seong, A.S. Om, J.Y. Yoon, Experimental investigation of the thermal and disinfection performances of a novel hydrodynamic cavitation reactor, Ultrason. Sonochem., 49 (2018) 13-23, https://doi.org/10.1016/j.ultsonch.2018.02.039.

[11] J. Mevada, S. Devi, A. Pandit, Large scale microbial cell disruption using hydrodynamic cavitation: Energy saving options, Biochem. Eng. J., 143 (2019) 151-160, https://doi.org/10.1016/j.bej.2018.12.010.

[12] H. Kim, X. Sun, B. Koo, J.Y. Yoon, Experimental Investigation of Sludge Treatment Using a Rotor-Stator Type Hydrodynamic Cavitation Reactor and an Ultrasonic Bath, Processes, 7 (2019), https://doi.org/10.3390/pr7110790.

[13] R. Terán Hilares, R.M. Dionízio, S. Sánchez Muñoz, C.A. Prado, R. de Sousa Júnior, S.S. da Silva, J.C. Santos, Hydrodynamic cavitation-assisted continuous pre-treatment of sugarcane bagasse for ethanol production: Effects of geometric parameters of the cavitation device, Ultrason. Sonochem., 63 (2020) 104931, https://doi.org/10.1016/j.ultsonch.2019.104931.

[14] J. Kosel, A. Šinkovec, M. Dular, A novel rotation generator of hydrodynamic cavitation for the fibrillation of long conifer fibers in paper production, Ultrason. Sonochem., 59 (2019) 104721, https://doi.org/10.1016/j.ultsonch.2019.104721.

[15] H. Pang, G. Ngaile, Formulation of SiO2/oil nanolubricant for metal forming using hydrodynamic cavitation, Proc. Inst. Mech. Eng. Pt. B: J. Eng. Manuf., (2020) 0954405420933120, https://doi.org/10.1177/0954405420933120.

[16] L. Albanese, A. Bonetti, L.P. D'Acqui, F. Meneguzzo, F. Zabini, Affordable Production of Antioxidant Aqueous Solutions by Hydrodynamic Cavitation Processing of Silver Fir (Abies alba Mill.) Needles., Foods, 8 (2019) 65, https://doi.org/10.3390/foods8020065.

[17] S. Zhou, X. Wang, X. Bu, M. Wang, B. An, H. Shao, C. Ni, Y. Peng, G. Xie, A novel flotation technique combining carrier flotation and cavitation bubbles to enhance separation efficiency of ultra-fine particles, Ultrason. Sonochem., 64 (2020) 105005, https://doi.org/10.1016/j.ultsonch.2020.105005.

[18] A.P. Nagalingam, H.K. Yuvaraj, S.H. Yeo, Synergistic effects in hydrodynamic cavitation abrasive finishing for internal surface-finish enhancement of additive-manufactured components, Additive Manufacturing, 33 (2020) 101110, https://doi.org/10.1016/j.addma.2020.101110.

[19] S.B. Gregersen, L. Wiking, K.B. Bertelsen, J. Tangsanthatkun, B. Pedersen, K.R. Poulsen, U. Andersen, M. Hammershøj, Viscosity reduction in concentrated protein solutions by hydrodynamic cavitation, Int. Dairy J., 97 (2019) 1-4, https://doi.org/10.1016/j.idairyj.2019.04.015.

[20] X. Sun, S. Chen, J. Liu, S. Zhao, J.Y. Yoon, Hydrodynamic Cavitation: A Promising Technology for Industrial-Scale Synthesis of Nanomaterials, Front. Chem., 8 (2020), https://doi.org/10.3389/fchem.2020.00259.

[21] X. Sun, X. Xuan, L. Ji, S. Chen, J. Liu, S. Zhao, S. Park, J.Y. Yoon, A.S. Om, A novel continuous hydrodynamic cavitation technology for the inactivation of pathogens in milk, Ultrason. Sonochem., 71 (2021) 105382, https://doi.org/10.1016/j.ultsonch.2020.105382.
[22] J. Yan, S. Ai, F. Yang, K. Zhang, Y. Huang, Study on mechanism of chitosan degradation with hydrodynamic cavitation, Ultrason. Sonochem., 64 (2020) 105046, https://doi.org/10.1016/j.ultsonch.2020.105046.
[23] Ž. Pandur, I. Dogsa, M. Dular, D. Stopar, Liposome destruction by hydrodynamic cavitation in comparison to chemical, physical and mechanical treatments, Ultrason. Sonochem., 61 (2020) 104826, https://doi.org/10.1016/j.ultsonch.2019.104826.
[24] S. Parthasarathy, T. Siah Ying, S. Manickam, Generation and Optimization of Palm Oil-Based Oil-in-Water (O/W) Submicron-Emulsions and Encapsulation of Curcumin Using a Liquid Whistle Hydrodynamic Cavitation Reactor (LWHCR), Ind. Eng. Chem. Res., 52 (2013) 11829-11837, https://doi.org/10.1021/ie4008858.
[25] I. Gonçalves, M. Martins, A. Loureiro, A. Gomes, A. Cavaco-Paulo, C. Silva, Sonochemical and hydrodynamic cavitation reactors for laccase/hydrogen peroxide cotton bleaching, Ultrason. Sonochem., 21 (2014) 774-781, https://doi.org/10.1016/j.ultsonch.2013.08.006.
[26] S. Rajoriya, S. Bargole, S. George, V.K. Saharan, P.R. Gogate, A.B. Pandit, Synthesis and characterization of samarium and nitrogen doped TiO2 photocatalysts for photo-degradation of 4-acetamidophenol in combination with hydrodynamic and acoustic cavitation, Sep. Purif. Technol., 209 (2019) 254-269, https://doi.org/10.1016/j.seppur.2018.07.036.
[27] K.-W. Jung, D.-S. Park, M.-J. Hwang, K.-H. Ahn, Decolorization of Acid Orange 7 by an electric field-assisted modified orifice plate hydrodynamic cavitation system: Optimization of operational parameters, Ultrason. Sonochem., 26 (2015) 22-29, https://doi.org/10.1016/j.ultsonch.2015.02.010.
[28] M. Gągol, E. Cako, K. Fedorov, R.D.C. Soltani, A. Przyjazny, G. Boczkaj, Hydrodynamic cavitation based advanced oxidation processes: Studies on specific effects of inorganic acids on the degradation effectiveness of organic pollutants, J. Mol. Liq., 307 (2020) 113002, https://doi.org/10.1016/j.molliq.2020.113002.
[29] R.H. Jawale, P.R. Gogate, Novel approaches based on hydrodynamic cavitation for treatment of wastewater containing potassium thiocyanate, Ultrason. Sonochem., 52 (2019) 214-223, https://doi.org/10.1016/j.ultsonch.2018.11.019.
[30] Y. Tao, J. Cai, X. Huai, B. Liu, A novel antibiotic wastewater degradation technique combining cavitating jets impingement with multiple synergetic methods, Ultrason. Sonochem., 44 (2018) 36-44, https://doi.org/10.1016/j.ultsonch.2018.02.008.
[31] S.B. Doltade, G.G. Dastane, N.L. Jadhav, A.B. Pandit, D.V. Pinjari, N. Somkuwar, R. Paswan, Hydrodynamic cavitation as an imperative technology for the treatment of petroleum refinery effluent, J. Water Process. Eng., 29 (2019) 100768, https://doi.org/10.1016/j.jwpe.2019.02.008.
[32] Z. Wu, S. Tagliapietra, A. Giraudo, K. Martina, G. Cravotto, Harnessing

cavitational effects for green process intensification, Ultrason. Sonochem., 52 (2019) 530-546, https://doi.org/10.1016/j.ultsonch.2018.12.032.
[33] X. Sun, J. Liu, L. Ji, G. Wang, S. Zhao, J.Y. Yoon, S. Chen, A review on hydrodynamic cavitation disinfection: The current state of knowledge, Sci. Total Environ., (2020) 139606, https://doi.org/10.1016/j.scitotenv.2020.139606.
[34] M. Gągol, A. Przyjazny, G. Boczkaj, Highly effective degradation of selected groups of organic compounds by cavitation based AOPs under basic pH conditions, Ultrason. Sonochem., 45 (2018) 257-266, https://doi.org/10.1016/j.ultsonch.2018.03.013.
[35] A. Waghmare, K. Nagula, A. Pandit, S. Arya, Hydrodynamic cavitation for energy efficient and scalable process of microalgae cell disruption, Algal Res., 40 (2019) 101496, https://doi.org/10.1016/j.algal.2019.101496.
[36] M. Nabi, G. Zhang, P. Zhang, X. Tao, S. Wang, J. Ye, Q. Zhang, M. Zubair, S. Bao, Y. Wu, Contribution of solid and liquid fractions of sewage sludge pretreated by high pressure homogenization to biogas production, Bioresour. Technol., 286 (2019) 121378, https://doi.org/10.1016/j.biortech.2019.121378.
[37] A.V. Mohod, P.R. Gogate, G. Viel, P. Firmino, R. Giudici, Intensification of biodiesel production using hydrodynamic cavitation based on high speed homogenizer, Chem. Eng. J., 316 (2017) 751-757, https://doi.org/10.1016/j.cej.2017.02.011.
[38] D. Panda, S. Manickam, Hydrodynamic cavitation assisted degradation of persistent endocrine-disrupting organochlorine pesticide Dicofol: Optimization of operating parameters and investigations on the mechanism of intensification, Ultrason. Sonochem., 51 (2019) 526-532, https://doi.org/10.1016/j.ultsonch.2018.04.003.
[39] J. Wang, X. Wang, P. Guo, J. Yu, Degradation of reactive brilliant red K-2BP in aqueous solution using swirling jet-induced cavitation combined with H2O2, Ultrason. Sonochem., 18 (2011) 494-500, https://doi.org/10.1016/j.ultsonch.2010.08.006.
[40] M.B. Mane, V.M. Bhandari, K. Balapure, V.V. Ranade, Destroying antimicrobial resistant bacteria (AMR) and difficult, opportunistic pathogen using cavitation and natural oils/plant extract, Ultrason. Sonochem., (2020) 105272, https://doi.org/10.1016/j.ultsonch.2020.105272.
[41] W.C. Kwon, J.Y. Yoon, Experimental study of a cavitation heat generator, Proc. Inst. Mech. Eng,, Part E, 227 (2013) 67-73, https://doi.org/10.1177/0954408912451535.
[42] M. Petkovšek, M. Mlakar, M. Levstek, M. Stražar, B. Širok, M. Dular, A novel rotation generator of hydrodynamic cavitation for waste-activated sludge disintegration, Ultrason. Sonochem., 26 (2015) 408-414, https://doi.org/10.1016/j.ultsonch.2015.01.006.
[43] A. Šarc, J. Kosel, D. Stopar, M. Oder, M. Dular, Removal of bacteria Legionella pneumophila, Escherichia coli, and Bacillus subtilis by (super)cavitation, Ultrason. Sonochem., 42 (2018) 228-236, https://doi.org/10.1016/j.ultsonch.2017.11.004.
[44] X. Sun, C.H. Kang, J.J. Park, H.S. Kim, A.S. Om, J.Y. Yoon, An experimental study on the thermal performance of a novel hydrodynamic cavitation reactor, Exp. Therm Fluid Sci., 99 (2018) 200-210,

https://doi.org/10.1016/j.expthermflusci.2018.02.034.
[45] X. Sun, X. Jia, J. Liu, G. Wang, S. Zhao, L. Ji, J. Yong Yoon, S. Chen, Investigation on the Characteristics of an Advanced Rotational Hydrodynamic Cavitation Reactor for Water Treatment, Sep. Purif. Technol., (2020) 117252, https://doi.org/10.1016/j.seppur.2020.117252.
[46] J. Kosel, M. Šuštaršič, M. Petkovšek, M. Zupanc, M. Sežun, M. Dular, Application of (super)cavitation for the recycling of process waters in paper producing industry, Ultrason. Sonochem., 64 (2020) 105002, https://doi.org/10.1016/j.ultsonch.2020.105002.
[47] M.P. Badve, T. Alpar, A.B. Pandit, P.R. Gogate, L. Csoka, Modeling the shear rate and pressure drop in a hydrodynamic cavitation reactor with experimental validation based on KI decomposition studies, Ultrason. Sonochem., 22 (2015) 272-277, https://doi.org/10.1016/j.ultsonch.2014.05.017.
[48] H. Kim, B. Koo, X. Sun, J.Y. Yoon, Investigation of sludge disintegration using rotor-stator type hydrodynamic cavitation reactor, Sep. Purif. Technol., 240 (2020) 116636, https://doi.org/10.1016/j.seppur.2020.116636.
[49] X. Sun, X. Xuan, Y. Song, X. Jia, L. Ji, S. Zhao, J. Yong Yoon, S. Chen, J. Liu, G. Wang, Experimental and numerical studies on the cavitation in an advanced rotational hydrodynamic cavitation reactor for water treatment, Ultrason. Sonochem., 70 (2021) 105311, https://doi.org/10.1016/j.ultsonch.2020.105311.
[50] ANSYS, ANSYS Fluent 18.2 theory guide., 2017.
[51] X. Sun, S. Kim, S.D. Yang, H.S. Kim, J.Y. Yoon, Multi-objective optimization of a Stairmand cyclone separator using response surface methodology and computational fluid dynamics, Powder Technol., 320 (2017) 51-65, http://dx.doi.org/10.1016/j.powtec.2017.06.065.
[52] D.C. Wilcox, Turbulence Modeling for CFD, 3rd ed., DCW Industries, California, 2006.
[53] F. Menter, M. Kuntz, R.B. Langtry, Ten years of industrial experience with the SST turbulence model, Turbulence, Heat and Mass Transfer, 4 (2003) 8,
[54] B. Ji, X.W. Luo, R.E.A. Arndt, X. Peng, Y. Wu, Large Eddy Simulation and theoretical investigations of the transient cavitating vortical flow structure around a NACA66 hydrofoil, Int. J. Multiphase Flow, 68 (2015) 121-134, https://doi.org/10.1016/j.ijmultiphaseflow.2014.10.008.
[55] F.R. Menter, Best Practice: Scale-Resolving Simulations in ANSYS CFD, ANSYS Germany GmbH, Otterfing, 2012,
[56] F.R. Menter, Two-Equation Eddy-Viscosity Turbulence Models for Engineering Applications, AIAA J., 8 (1994) 8, https://doi.org/10.2514/3.12149
[57] G. Schnerr Professor Dr.-Ing.habil, Physical and Numerical Modeling of Unsteady Cavitation Dynamics, in: 4th International Conference on Multiphase Flow, New Orleans, La, USA, 2001.
[58] X. Sun, X. Jia, J. Liu, G. Wang, S. Zhao, L. Ji, J. Yong Yoon, S. Chen, Investigation on the Characteristics of an Advanced Rotational Hydrodynamic Cavitation Reactor for

Water Treatment, Sep. Purif. Technol., 251 (2020) 117252, https://doi.org/10.1016/j.seppur.2020.117252.
[59] P.J. Milly, R.T. Toledo, M.A. Harrison, D. Armstead, Inactivation of Food Spoilage Microorganisms by Hydrodynamic Cavitation to Achieve Pasteurization and Sterilization of Fluid Foods, J. Food Sci., 72 (2007) M414-M422, https://doi.org/10.1111/j.1750-3841.2007.00543.x

[60] M. Badve, P. Gogate, A. Pandit, L. Csoka, Hydrodynamic cavitation as a novel approach for wastewater treatment in wood finishing industry, Sep. Purif. Technol., 106 (2013) 15-21, https://doi.org/10.1016/j.seppur.2012.12.029.
[61] M.P. Badve, P.R. Gogate, A.B. Pandit, L. Csoka, Hydrodynamic cavitation as a novel approach for delignification of wheat straw for paper manufacturing, Ultrason. Sonochem., 21 (2014) 162-168, https://doi.org/10.1016/j.ultsonch.2013.07.006.
[62] P. Chipurici, A. Vlaicu, I. Calinescu, M. Vinatoru, M. Vasilescu, N.D. Ignat, T.J. Mason, Ultrasonic, hydrodynamic and microwave biodiesel synthesis – A comparative study for continuous process, Ultrason. Sonochem., 57 (2019) 38-47, https://doi.org/10.1016/j.ultsonch.2019.05.011.
[63] B. Maršálek, Š. Zezulka, E. Maršálková, F. Pochylý, P. Rudolf, Synergistic effects of trace concentrations of hydrogen peroxide used in a novel hydrodynamic cavitation device allows for selective removal of cyanobacteria, Chem. Eng. J., 382 (2020) 122383, https://doi.org/10.1016/j.cej.2019.122383.
[64] P.N. Patil, P.R. Gogate, L. Csoka, A. Dregelyi-Kiss, M. Horvath, Intensification of biogas production using pretreatment based on hydrodynamic cavitation, Ultrason. Sonochem., 30 (2016) 79-86, https://doi.org/10.1016/j.ultsonch.2015.11.009.
[65] P.J. Milly, R.T. Toledo, W.L. Kerr, D. Armstead, Hydrodynamic Cavitation: Characterization of a Novel Design with Energy Considerations for the Inactivation of Saccharomyces cerevisiae in Apple Juice, J. Food Sci., 73 (2008) M298-M303, https://doi.org/10.1111/j.1750-3841.2008.00827.x.

Declaration of interests

☒ The authors declare that they have no known competing financial interests or personal relationships that could have appeared to influence the work reported in this paper.

☐The authors declare the following financial interests/personal relationships which may be considered as potential competing interests:

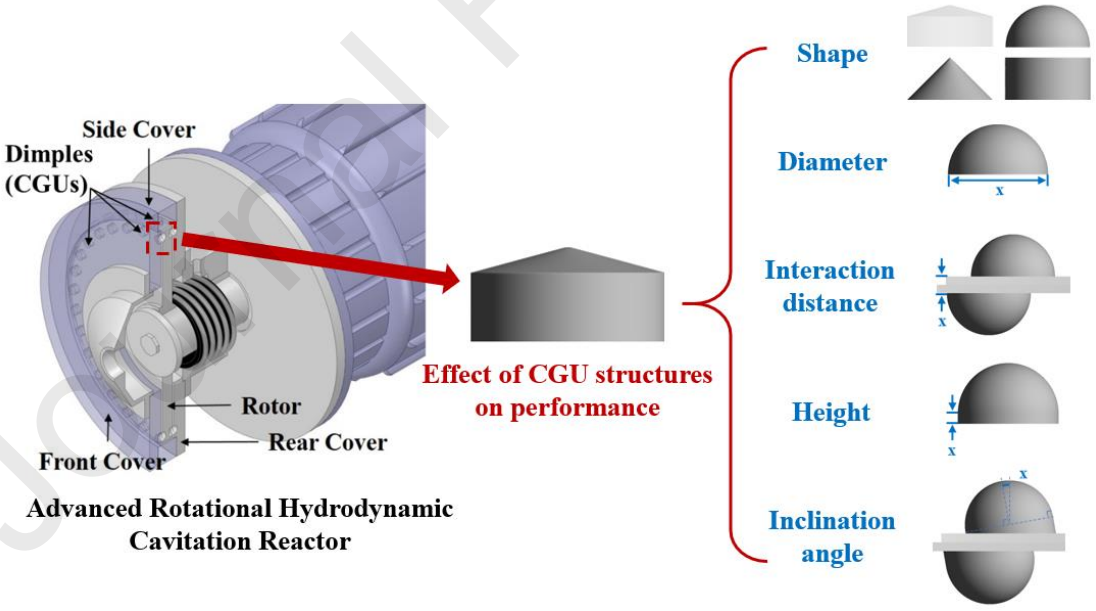

Highlights

- Effects of CGU structure on ARHCR performance are studied by CFD.
- ARHCRs with rotor-stator interactions are far superior to non-interaction ones.

- Hemisphere-shaped CGUs show the best performance among other common structures.
- Effects of diameter, distance, height, and inclination angle are revealed.
- This work offers a viable way to design high-performance ARHCRs.